

Tidal effects in gravitational waves from neutron stars in scalar-tensor theories of gravity

Gastón Creci,^{1,*} Iris van Gemeren,^{1,†} Tanja Hinderer,¹ and Jan Steinhoff²

¹*Institute for Theoretical Physics, Utrecht University,
Princetonplein 5, 3584 CC Utrecht, Netherlands, European Union*
²*Max-Planck-Institute for Gravitational Physics (Albert-Einstein-Institute),
Am Mühlenberg 1, 14476 Potsdam-Golm, Germany, European Union*

(Dated: December 10, 2024)

We compute tidal signatures in the gravitational waves (GWs) from neutron star binary inspirals in scalar-tensor gravity, where the dominant adiabatic even-parity tidal interactions involve three types of Love numbers that depend on the matter equation of state and parameters of the gravitational theory. We calculate the modes of the GW amplitudes and the phase evolution in the time and frequency domain, working up to first order in the post-Newtonian and small finite-size approximations. We also perform several case studies to quantify the dipolar and quadrupolar tidal effects and their parameter dependencies specialized to Gaussian couplings. We show that various tidal contributions enter with different signs and scalings with frequency, which generally leads to smaller net tidal GW imprints than for the same binary system in General Relativity.

CONTENTS

I. Introduction	1	D. Identifying interesting parameter regimes	15
II. Setup and approximation scheme for neutron star binary inspirals in ST theories	2	E. Tidal effects on the GW phase evolution	18
A. Scalar-tensor theories of gravity	2	VI. Summary and Conclusion	21
B. Relevant scales for binary neutron star systems in ST theories	3	VII. Acknowledgements	22
C. Overview of the approach to compute tidal GW signatures in ST theories	5	A. Useful identities involving symmetric trace-free tensors	23
D. Skeletonized action including tidal effects	5	B. Full expressions for the binary dynamics, waveforms and GW phase	23
E. Field equations derived from the action	5	C. Ready-to-use expressions for the tidal coefficients in the phase	27
III. Binary dynamics in the PN and tidal approximations	6	1. Quadrupolar-driven regime	27
A. Near zone fields and two body dynamics	6	2. Dipolar-driven regime	28
B. Tidal contributions to the reduced two-body Lagrangian and relative acceleration	7	D. Gravitational waves in Jordan frame from Einstein frame results	28
C. Tidal contributions to the binding energy	7	1. Derivation based on the short-wave approximation	28
IV. Tidal effects in the scalar and gravitational radiation	8	2. Derivation beyond the short-wave approximation	30
A. Tidal contributions to the scalar waveform	8	E. Elaboration on the parameter space study	31
B. Tidal contributions to the tensor waveform	9	F. Dipolar Driven phase evolution	33
C. Gravitational waves in the Jordan frame	9	References	33
D. Energy fluxes	10		
E. GW phase evolution	11		
V. Case study of neutron star binaries	12		
A. Set-up and properties of single neutron stars	12		
B. Computation of $\beta(\varphi)$	13		
C. Waveform and frequency evolution of example binary systems	15		

I. INTRODUCTION

Gravitational waves (GWs) are copiously produced by coalescing compact binary systems, with more than ninety confirmed detections to date [1–3] that have already yielded valuable insights into these sources and dynamical spacetime itself. Systems involving neutron

* g.f.crecikeinbaum@uu.nl

† i.r.vangemeren@uu.nl

stars (NSs) [4–7] are particularly rich in information because they involve strong-field gravity coupled to subatomic matter at supranuclear densities, which remains a longstanding frontier in nuclear physics [8–10]. Extracting this information from GW signals relies on template models used for the detection and parameter estimation analysis. Shortcomings of the templates can thus jeopardize the interpretation of our measurements. This has motivated a significant research efforts to improve the accuracy and physical realism of theoretical models. While theory-agnostic tests of gravity are most commonly used in data analysis, and have already provided constraints on parameterized deviations of the measured waveforms from those in General Relativity (GR) [11–13], complementary theory-specific calculations are needed to connect between empirical measurements and fundamental theory, and to potentially reveal new phenomena to search for.

In this paper, we study GW signatures from tidal effects in NS binary inspirals in scalar-tensor (ST) theories of gravity [14–17]. Such theories involve a scalar field coupled to the metric, which can give rise to *scalarized* NS solutions whose internal structure depends on the scalar field [15, 18–24]. We consider here ST theories in which scalarization of isolated NSs occurs only when their compactness is above a parameter-dependent critical value [15, 19, 20], while black holes and less compact stars are unaltered compared to GR. Thus, ST theories avoid the stringent constraints on deviations from GR imposed by Solar-system experiments [25], but are constrained by observations of binary pulsar, where scalar radiation would lead to accelerated orbital decay relative to GR [19, 26–30]. Complementary constraints come from GW measurements, where scalar radiation and other modifications of the inspiral as well as phenomena such as dynamical scalarization [31], whereby an unscalarized star can become scalarized when reaching a certain separation from the companion, could also play a role [32–39].

The effects of scalarization on a NS’s internal structure are encoded in the GW signals, for example, through tidal deformability coefficients that characterize the ratio of the star’s induced multipole moments to tidal fields due to the binary companion [40–44]. In ST theories, this induced response for each multipolar order and even parity comprises three different tidal deformabilities [45] in contrast to only one parameter for NSs in GR. This arises because mass and scalar quadrupoles are induced by the gravitational and scalar tidal fields respectively, and moreover, the nonlinear interplay between gravity and matter also results in an induced scalar multipole in response to a tensor tidal field and vice versa. These tidal deformabilities are sensitive to the still poorly constrained equation of state (EoS) of NS matter as well as properties of the scalar field and spacetime [5, 46–50]. While we consider here a specific class of ST theories, our methods have broader applicability to other theories of gravity where scalarized NSs can arise.

There has been much previous work on understanding and modeling the effects of ST gravity on GW signals from binary inspirals. A number of numerical studies of NS binaries in ST theories have analyzed or revealed features due to scalarization, such as the black-hole NS simulations of [51] and those of binary NS mergers in [24, 31, 52, 53]. Analytical waveforms have been computed in ST theories up to 1.5PN order [18, 32, 48, 54–67]. The leading order dipolar tidal effects in the scalar sector have also been modeled [48, 68].

In this paper, we complement existing work by assessing the importance of tidal effects up to quadrupolar order. We compute the different tidal contributions to the Fourier and time-domain waveform, working to linear order in finite-size effects and to 1PN order in relativistic effects on the orbital scale. We survey the parameter space of the effects and select several fiducial binary systems that maximize some of these effects as well as intermediate cases whose GW signals we analyze in detail, with particular focus on the GW phasing due to the different kinds of tidal effects.

The paper is organized as follows. In Section II, we start by discussing GWs in ST theories, their transformations between different computational frames often used in literature, and the effective action description of a compact binary system. In Section III, we derive the leading tidal effects to 1PN results and compute the waveforms. In Sec. V, we apply our results to scalarized NS considering three EoS ranging from stiff to soft and discuss our findings. We finish with the conclusion and outlook in Sec. VI. We leave the details concerning the PN calculations and our parameter space study to Appendix B and E, respectively.

The notation and conventions we use are the following. Greek letters α, β, \dots denote spacetime indices, while Latin indices i, j, \dots correspond to spatial components. We use ∇_μ to denote the covariant derivative and ∂_μ for the partial derivative. Capital-letter super and subscripts, with the exception of the labels T, S and ST, correspond to a string of indices on a tensor (see e.g. [69] for details), and angular brackets on tensor indices denote the symmetric and trace-free (STF) part. For instance, for a unit three-vector n^i , the STF tensor $n_{\langle L=2 \rangle} = n_i n_j - 1/3 \delta_{ij}$, with δ_{ij} the Kronecker delta. We adopt the Einstein summation convention on all types of indices, i.e., any repeated indices are summed over. In this work we set the speed of light equal to unity; $c = 1$.

II. SETUP AND APPROXIMATION SCHEME FOR NEUTRON STAR BINARY INSPIRALS IN ST THEORIES

A. Scalar-tensor theories of gravity

Scalar-tensor theories are a class of theories beyond GR that include a scalar field coupled with the metric. The action for such theories can be formulated in two

frames. Historically, it was first formulated in the so-called Jordan frame,

$$S_{\text{ST}}^{(\text{J})} = \int_{\mathcal{M}} d^4x \frac{\sqrt{-g_*}}{16\pi G} \left[F(\phi) R_* - \frac{\omega(\phi)}{\phi} \partial^\mu \phi \partial_\mu \phi - V(\phi) \right] + S_{\text{matter}} [\psi_m, g_{\mu\nu}^*], \quad (2.1)$$

with R_* the Ricci scalar, $F(\phi)$ an arbitrary function of the scalar field ϕ , $\omega(\phi)$ a self-interaction coupling, and $V(\phi)$ its potential. The asterisk is only a notational adornment to distinguish quantities from those associated to a conformal metric introduced below. In this work, we will focus on massless scalar fields, so that $V(\phi) = 0$. We note that in (2.1), the scalar couples only to the curvature while the matter part is the same as in GR; in particular, there are no effects on the particle physics of the standard model. However, the scalar coupling to the curvature leads to complicated equations of motion for the metric fields. Thus, it is convenient to transform to a different frame where the field equations simplify. Specifically, by performing a conformal transformation

$$g_{\mu\nu}^* = A(\varphi)^2 g_{\mu\nu}, \quad (2.2)$$

with a field-dependent conformal factor that is related to the coupling function by

$$A(\varphi) = \exp \left(- \int d\varphi \frac{F'}{2F\sqrt{\Delta}} \right), \quad (2.3)$$

where φ is defined by the field redefinition,

$$\frac{d\varphi}{d\phi} = \sqrt{\Delta}, \quad (2.4a)$$

$$\partial_\alpha \phi = \frac{1}{\sqrt{\Delta}} \partial_\alpha \varphi, \quad (2.4b)$$

with

$$\Delta \equiv \frac{3}{4} \left(\frac{F'}{F} \right)^2 + \frac{1}{2} \frac{\omega(\phi)}{\phi F}, \quad (2.5)$$

and a prime denoting a derivative with respect to the argument, $F' = dF/d\phi$, we obtain the action in the Einstein frame,

$$S_{\text{ST}}^{(\text{E})} = \int_{\mathcal{M}} d^4x \frac{\sqrt{-g}}{16\pi G} [R - 2g^{\mu\nu} \partial_\mu \varphi \partial_\nu \varphi] + S_{\text{matter}} [\psi_m, A^2(\varphi) g_{\mu\nu}]. \quad (2.6)$$

In the Einstein frame, the gravitational sector of the action is the Ricci scalar R associated to the metric $g_{\mu\nu}$ with a free scalar field φ . However, the matter action contains $A(\varphi)$ which couples the metric and scalar field through the matter action. In principle, as the two frames differ only by a conformal transformation, any measurable quantities should be independent of the choice of frame, provided that they are calculated consistently within each frame.

B. Relevant scales for binary neutron star systems in ST theories

We first consider relevant scales involved in the problem to gain insight into the basic physics dominating different aspects of the binary dynamics and GWs and to define appropriate approximation schemes to model them. Specifically, we consider two non-spinning NSs or a black hole-NS system at large separation r during their early inspiral. Due to the presence of the scalar field in the gravitational theory, depending on the parameters, a scalar configuration inside and around NSs can arise [18]. We assume the binary to move in a quasi-circular motion, slowly decreasing in radius due to the loss of GWs and scalar radiation. Fig. 1 shows a schematic illustration of the systems we consider. The smallest scale that is rel-

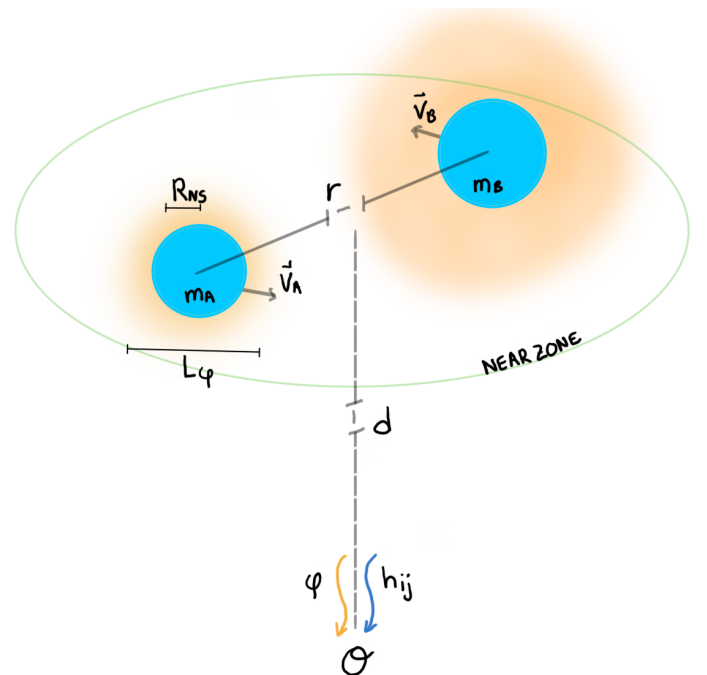


FIG. 1. Schematic illustration of the binary systems of NS A and B and their respective masses and velocities. The relevant length scales of the system are labelled.

evant for modeling the GWs is the size of the bodies in the binary. For a black hole, this is of the order of its Schwarzschild radius $r_S \sim 2GM$, with M its mass, while for NSs, depending on its mass and EoS, it is generally of order $R_{\text{NS}} \sim O(10\text{km})$ equivalent to a few times r_S . During the early inspiral, the orbital separation r is much larger than the size of the bodies, $r \gg R_{\text{body}}$. The next larger scale in this setup is the reduced wavelength of the GWs, which is of order $\omega_{\text{GW}}^{-1} \sim O(\omega^{-1})$ with ω the orbital angular frequency. The largest scale is the distance from the source to the observer denoted by d . The above scales are commonly discussed in the literature on PN theory and finite size effects in binary systems in GR, as

reviewed e.g. in [70].

In beyond-GR gravity theories, it is often the case that the presence of extra fields introduce new scales into the problem. However, in the massless ST theories we consider here, the scalar configuration (in cases where it exists) is given by a monotonically decreasing function outside the star, in principle extending to infinity. To be able to still assign a characteristic length scale to the scalar configuration we look at the ADM energy of the field

$$E^\varphi = \int_{\mathcal{S}} \sqrt{\gamma} d^3x n^\alpha T_{\alpha\beta} t^\beta, \quad (2.7)$$

where t^β is the timelike Killing vector $\vec{\partial}/\partial t$, \mathcal{S} the spatial hypersurface with induced metric $\gamma_{\alpha\beta}$ and n^α is the timelike unit normal. The neutron star background metric is obtained by solving the ST field equations with a matter action corresponding to the perfect fluid energy momentum tensor. For details we refer to Sec. V A 2 and [45]. The energy momentum tensor of the scalar field will be introduced at the end of this section in (2.19). Fig. 2 shows the percentage of the scalar field ADM energy as function of the radial distance for an example case NS of $1.4M_\odot$, assuming EoS SLy and ST parameter $\beta_0 = -4.5$. We give a more detailed discussion on the possible parameter choices in Sec. V. In this case, we find that the ADM energy around the scale of $\sim 5.5R_{NS}$ is around 90% of the total ADM energy at spatial infinity. We repeated this analysis for a range of NS masses and respectively softer to stiffer EoS WFF1, SLy, H4 and for different values of the ST parameter β_0 . For this sweep of the parameter space we found very similar profiles for the ADM energy percentage as shown in Fig. 2 for which 90% of the total ADM energy is always captured in a region smaller than $\mathcal{O}(10)R_{\text{body}}$. Hence despite of the slow falloff of the scalar field itself, its energy is concentrated in a region close to the body. There are no strict criteria for defin-

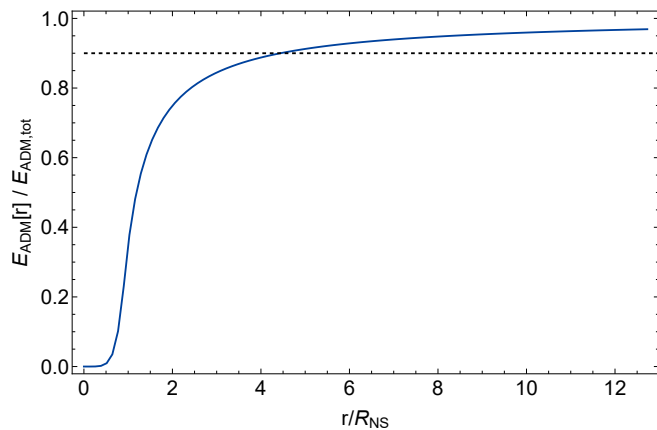


FIG. 2. Ratio of the ADM energy as function of the radial distance over the total ADM energy at large distances for a NS of $1.4M_\odot$, considering the SLy EoS and $\beta_0 = -4.5$. The dashed line corresponds to a ratio of 0.9.

ing the scale of the scalar configuration. However in the

overall hierarchy of scales we discuss in this section based on Fig. 2 we can say it is of the order of magnitude of R_{body} . We define therefore the characteristic length scale of the scalar cloud to be

$$L_\varphi \sim 6R_{\text{body}}. \quad (2.8)$$

Even though the ADM energy related to the scalar field is concentrated close to the compact object, the energy density at the relevant scales during the inspiral can still be significant. To get some insight we did an order of magnitude estimate regarding the density of the field. At a GW frequency around 200Hz during the inspiral part of a coalescing event of a NS binary, their relative distance can be found via $r \sim f\pi/G\alpha M$, with α a ST parameter related to the scalar charges of the NSs, defined in (3.7), and M the total mass of the binary system. We derive this explicitly in (B6). At this radial distance we find the energy density of the scalar field corresponding to the 00 component of the scalar energy momentum tensor (2.19) to be $\mathcal{O}(10^{11})\text{kg/m}^3$. This is computed for an equal mass NS system of $1.4M_\odot$ with EoS SLy and $\beta_0 = -4.5$. This density surpasses white dwarf like energy densities. For fields with large energy densities, environmental effects like dynamical friction (DF) can leave a significant imprint on the GW signature. The energy loss due to dynamical friction during the inspiral is given by [71, 72]

$$\mathcal{F}_{DF} \sim 4\pi\rho\eta^2 \frac{G^2 M^2}{v} \ln \Lambda, \quad (2.9)$$

with ρ the scalar field energy density, $\eta = m_1 m_2 / M^2$ the symmetric mass ratio, $v \sim \sqrt{GM/r}$ the velocity of the body moving through the field, which we approximate by the Keplerian velocity. $\ln \Lambda$ denotes the Coulomb algorithm characterized by the impact parameters of the two body encounters. As our order of magnitude is not sensitive to the estimate of Λ and it is usually $\mathcal{O}(1)$ [72] we will set it to unity for this estimate. Comparing the DF energy loss to the GW leading order energy flux $\mathcal{F}_{GW} \sim 32/5 G^4 \eta^2 (M/r)^5$ we find the ratio of the fluxes at GW frequency 200Hz to be

$$\frac{\mathcal{F}_{DF}}{\mathcal{F}_{GW}} \sim \mathcal{O}(10^{-1}). \quad (2.10)$$

Hence the effect of DF on the GWs due to the presence of the scalar field can become quite significant during the inspiral, moving towards higher energy densities when the radial distance shrinks. We highlight therefore the importance of incorporating environmental effects due to the additional scalar field in future work.

To come back to our discussion on the hierarchy of the length scales in the system as shown in Fig. 1, we divide the problem into different zones. The near zone is defined by $r_{NZ} \ll \omega_{\text{GW}}^{-1}$ [73] which captures physics on the orbital scale. The far zone encompasses the region outside the near-zone. In the two zones we use different approximation schemes and match them in the intermediate region. The approximation methods adapted to the

different zones are based on expansions in small dimensionless parameters. Finite size effects are characterized by the ratio between the body scale and the orbital separation

$$\epsilon_{tid} \sim \frac{R_{\text{body}}}{r} \ll 1. \quad (2.11)$$

As discussed above, for the scalar tidal effects we also work in the approximation that $(L_\varphi/r) \ll 1$. Furthermore the PN weak field and slow motion parameter is

$$\epsilon_{PN} \sim \frac{GM}{r} \sim v^2 \ll 1. \quad (2.12)$$

We use these parameters to define perturbative expansions that enable us to compute explicit results for the dynamics and GWs of NS binaries in ST theories including tidal effects.

C. Overview of the approach to compute tidal GW signatures in ST theories

Our calculation in the sections below is structured as follows. We start with a computation of the orbital dynamics on the scale of the relative separation of the two bodies. Because of this large separation relative to their size, the objects can be described by point particles with small corrections due to their finite size and the scalar condensate. These are described by the introduction of a scalar dependent mass and tidally induced multipole moments. We expand the field equations from action (2.6) perturbatively to first order in ϵ_{PN} and ϵ_{tid} which are small in the near zone. This is followed by a computation of the waveforms at the detector, here one can expand in the large distance to the source d , resulting in a multipolar decomposition of the fields. We obtain the waveforms and GW phase in terms of the global characteristics of the objects. We can relate these parameters to the fundamental properties of the bodies by using the results on the tidal properties for NSs in scalar-tensor theories of [45].

D. Skeletonized action including tidal effects

When studying the relativistic two-body problem during the early inspiral, we can take advantage of the hierarchy of scales to formulate an effective description valid at the scale of interest. Here, we are interested in the early inspiral where the separation between the bodies r is larger than their characteristic size R , $R/r \ll 1$. To describe the binary system on the large scales of the orbital dynamics and the radiation we make the approximation that the worldtubes of each of the bodies reduce to a fiducial worldline, corresponding to a point-particle at their center of mass, augmented by an infinite sum of

multipole moments describing finite-size effects¹. In this approximation, the total matter action has the form

$$S_{\text{matter}}[g_{\mu\nu}, \varphi, x_A^\mu] = S_{\text{pp}} + S_{\text{tid}}, \quad (2.13)$$

with

$$S_{\text{pp}} = - \int d\tau z m(\varphi), \quad (2.14)$$

the point-particle action with a field-dependent mass $m(\varphi)$, which accounts for the fact that free falling bodies acquire scalar-field dependent terms, therefore violating the strong equivalence principle [56], and $z = \sqrt{-u_\mu u^\mu}$ the redshift factor. For the finite-size effects, we consider here only static tidally-induced scalar and tensor multipole moments of the form

$$Q_L^S = -\lambda_S^\ell E_L^S - \lambda_{ST}^\ell E_L^T, \quad (2.15a)$$

$$Q_L^T = -\lambda_T^\ell E_L^T - \lambda_{ST}^\ell E_L^S, \quad (2.15b)$$

where $E_L^{S/T}$ are scalar and tensor tidal fields given by

$$\begin{aligned} E_L^S &= -\nabla_L \varphi, \\ E_L^T &= \frac{1}{z^2} \nabla_{L-2} C_{a_1 a_2 \beta} u^\alpha u^\beta, \end{aligned} \quad (2.16)$$

where $C_{\mu\alpha\nu\beta}$ is the Weyl tensor, u^α the four-velocity tangent to the worldline, and the indices L are taken to run over a_1, a_2, \dots, a_ℓ , with ℓ the multipolar order. The tidal deformability or Love number coefficients $\lambda_{S/T/ST}^\ell$ characterize the various tidal responses of the star. They contain information from the strong-field regime inside the stars. For the class of ST theories considered in [45], the scalar-tensor Love numbers λ_{ST}^ℓ were found to be negative, while λ_S and λ_T were positive. From (2.15), this implies that the deformation of the star characterized by λ_{ST} is of the opposite sign compared to the pure scalar or tensor response.

Using the above definitions, the action for linear, static, even-parity tidal effects is given by [45]

$$\begin{aligned} S_{tid} &= \sum_\ell \int d\tau z g^{LP} \times \\ &\left(\frac{\lambda_S^\ell}{2\ell!} E_L^S E_P^S + \frac{\lambda_T^\ell}{2\ell!} E_L^T E_P^T + \frac{\lambda_{ST}^\ell}{\ell!} E_L^T E_P^S \right). \end{aligned} \quad (2.17)$$

E. Field equations derived from the action

The total action for the system consists of the gravitational action, for which we use the Einstein-frame action (2.6), together with the skeletonized description of

¹ Recall that a multipolar series expands in powers of R/r .

the two bodies (2.14). Varying with respect to the dynamical fields results in the following field equations

$$G_{\mu\nu} = 2T_{\mu\nu}^{\varphi} - 8\pi G(T_{\mu\nu}^{pp} + T_{\mu\nu}^{tid}), \quad (2.18)$$

with

$$G_{\mu\nu} = R_{\mu\nu} - \frac{1}{2}Rg_{\mu\nu}, \quad (2.19)$$

$$T_{\mu\nu}^{\varphi} = \nabla_{\mu}\varphi\nabla_{\nu}\varphi - \frac{1}{2}g_{\mu\nu}\nabla_{\rho}\varphi\nabla^{\rho}\varphi. \quad (2.20)$$

the Einstein tensor and scalar field energy momentum tensor respectively. Furthermore we define

$$T_{\mu\nu}^{pp} = \frac{-2}{\sqrt{-g}}\frac{\delta S_{pp}}{\delta g^{\mu\nu}}, \quad T_{\mu\nu}^{tid} = \frac{-2}{\sqrt{-g}}\frac{\delta S_{tid}}{\delta g^{\mu\nu}}, \quad (2.21)$$

as the energy momentum tensors associated to the point-particle and tidal action. It is useful to work with the trace-reversed form of the field equations

$$R_{\mu\nu} - 2\nabla_{\mu}\varphi\nabla_{\nu}\varphi + 8\pi G(T_{\mu\nu}^{pp} - \frac{1}{2}g_{\mu\nu}T^{pp}) + 8\pi G(T_{\mu\nu}^{tid} - \frac{1}{2}g_{\mu\nu}T^{tid}) = 0. \quad (2.22)$$

where the trace of the energy momentum tensor is given by $T^{pp} = g^{\alpha\beta}T_{\alpha\beta}^{pp}$ and similarly for the tidal part. The field equation for the scalar field results in

$$\frac{1}{4\pi G}\square\varphi = -\frac{1}{\sqrt{-g}}\frac{\delta S_m}{\delta\varphi}, \quad (2.23)$$

where $\square \equiv g^{\alpha\beta}\nabla_{\alpha}\nabla_{\beta}$ denotes the d'Alembertian operator.

III. BINARY DYNAMICS IN THE PN AND TIDAL APPROXIMATIONS

To solve the equations of motion we work perturbatively to linear order in tidal effects and in the post-Newtonian (PN) approximation for relativistic effects to relative 1PN order throughout. The point-particle effects are already known to 1.5 Post-Newtonian (PN) order [18, 63, 64, 67]. Tidal effects from dipolar scalar effects have also been computed [68]. As we work in the Einstein frame, our results also resemble those in scalar-Gauss-Bonnet gravity in the zero coupling limit [49, 74, 75]. We do not discuss the known results in detail here and instead focus on the new kinds of tidal contributions at higher multipolar order. We collect the total 1PN and tidal corrections of the dynamics, waveforms and phase evolution in Appendix B.

A. Near zone fields and two body dynamics

To construct the tidal contributions to the dynamics of a two body system, we rely on a double perturbative expansion in the PN approximation characterized by the

small parameter (2.12) and in the tidal corrections characterized by (2.11) and the scalar analogue. We assume each of these corrections to be small and treat them as independent. We focus on the contributions to linear order in the tidal expansion and in the PN approximation. Cross terms of $O(\epsilon_{PN}\epsilon_{tid})$ are discarded as being of higher order in smallness.

In the PN approximation, the metric is expanded around flat spacetime and the scalar field around its background value. For convenience, we henceforth use $\epsilon_{PN} \rightarrow v^2$ as the PN expansion parameter. To 1PN order, the metric and scalar have the expansion

$$g_{00} = e^{-2U} + \mathcal{O}(v^6), \quad (3.1a)$$

$$g_{0i} = -4g_i + \mathcal{O}(v^5), \quad (3.1b)$$

$$g_{ij} = \delta_{ij}e^{2U} + \mathcal{O}(v^4), \quad (3.1c)$$

$$\varphi = \varphi_0 + \delta\varphi^{(1)} + \mathcal{O}(v^4). \quad (3.1d)$$

From (3.1d) it also follows that the scalar-dependent mass of body A has the expansion

$$m_A(\varphi) = M_A \left\{ 1 + q_A\delta\varphi_A^{(1)} + \left(q_A\delta\varphi_A^{(2)} + \frac{1}{2}[(q_A)^2 + \beta_A]\delta\varphi_A^{(1)2} \right) \right\} + \mathcal{O}(v^6), \quad (3.2a)$$

with M_A the ADM mass, q_A the scalar charge, and β_A its derivative

$$q_A = \left. \frac{d \log m_A(\varphi)}{d\varphi} \right|_{\varphi=\varphi_0}, \quad \beta_A = \left. \frac{d q_A(\varphi)}{d\varphi} \right|_{\varphi=\varphi_0}. \quad (3.2b)$$

The identification of the expansion coefficients in (3.2a) with the properties of a potentially scalarized NS comes from matching the skeletonized description to the full theory, as discussed in [74]. We adopt the convention from [18] to write the corrections to the mass in terms of the scalar charge instead of the sensitivity parameter $s_A = (d \log m_A(\varphi)/d \log \varphi)|_{\varphi=\varphi_0}$ that is also often used in the literature [63, 65, 67]. For the conversion between the charge and sensitivity and other constituent parameters, we refer to Appendix A of [64].

Additionally, the fields in (3.1) are expanded to first order in tidal corrections. However, as was studied in Appendix B of [49], the tidal contributions to the field equations first enter at 1PN order. Here we discard these contributions as higher order, as we focus on the leading Newtonian order tidal corrections. Therefore after substituting the expanded metric (3.1) and mass (3.2a) in the field equations (2.22), (2.23), and solving the equations for the fields order by order in the PN expansion, we recover the lowest order contributions of the near zone fields [49, 63, 75]

$$U = \frac{GM_A}{r} + (A \leftrightarrow B) + \mathcal{O}(v^4), \quad (3.3)$$

$$\delta\varphi^{(1)} = -\frac{GM_A q_A}{r} + (A \leftrightarrow B) + \mathcal{O}(v^4),$$

where r is the relative separation between the bodies. As these field solutions are obtained in the PN approximation they are only valid in the near zone region introduced in Sec. II B. For the tidal corrections we focus on the leading order corrections in a Newtonian order gravitational background, where (2.16) reduces to

$$\begin{aligned} E_{L,A}^S &= -\partial_L \varphi = GM_A q_A \partial_L \left(\frac{1}{r} \right) \\ &= GM_A q_A \frac{(-1)^\ell r_{<L>^A} (2\ell - 1)!!}{r^{(2\ell+1)}}, \end{aligned} \quad (3.4a)$$

here $r_{<L>}$ denotes the symmetric trace free (STF) product of L radial terms. For the tensor tidal fields we have

$$\begin{aligned} E_{L,A}^T &= -\partial_L U = -GM_A \partial_L \left(\frac{1}{r} \right) \\ &= -GM_A \frac{(-1)^\ell r_{<L>^A} (2\ell - 1)!!}{r^{(2\ell+1)}}. \end{aligned} \quad (3.4b)$$

We note that the scalar charge q_A is negative [45], which makes both kinds of fields in (3.4) of the same sign for a fixed multipolar order ℓ . To derive (3.4), we substituted the near zone fields (3.3) into the general expressions (2.16), used the identity (A1) for ℓ derivatives of $1/r$ and defined $r_{<L>}^A = (x_A - x_B)^{<L>}$, with x_A^i and x_B^i the components of the position vectors of body A and B , respectively.

B. Tidal contributions to the reduced two-body Lagrangian and relative acceleration

To construct the tidal contributions to the binary dynamics, we start by substituting the PN expansions for the mass (3.2a) and tidal fields (3.4) in (2.14) and (2.17) and obtain the following tidal contributions to the Lagrangian

$$\frac{dS_{tid}^A}{dt} = G^2 M_A^2 \sum_{\ell} \frac{(2\ell - 1)!!}{2r^{2(\ell+1)}} (\lambda_{T,A}^{\ell} + \lambda_{S,A}^{\ell} q_B^2 - 2\lambda_{ST,A}^{\ell} q_B) \quad (3.5)$$

where we used the identity (A2) for the contraction of STF unit vectors. Adding the contributions from both bodies yields

$$L_{tid} = G^2 \mu M \alpha^2 \sum_{\ell} \frac{(2\ell - 1)!!}{2r^{2(\ell+1)}} \zeta_{\ell}, \quad (3.6)$$

with

$$\alpha \equiv 1 + q_A q_B, \quad (3.7)$$

$M = M_A + M_B$ the total mass, $\mu = M_A M_B / M$ the reduced mass and a combination of tidal parameters

$$\zeta_{\ell} \equiv \frac{M_A}{M_B \alpha^2} [\lambda_{T,B}^{\ell} + \lambda_{S,B}^{\ell} q_A^2 - 2\lambda_{ST,B}^{\ell} q_A] + (A \leftrightarrow B). \quad (3.8)$$

This tidal contribution adds linearly to the point-mass Lagrangian. The total two-body Lagrangian up to 1PN is given by (B1). The expressions for the tidal Lagrangian and acceleration are structurally the same as in GR, where only a tensor deformability appears. Hence, all three Love numbers in ST theories can be taken into account substituting $\zeta_{\ell}^{\text{GR}} \rightarrow \zeta_{\ell}^{\text{ST}}$.

From the two-body Lagrangian we compute the relative acceleration from the Euler-Lagrange equations in relative form

$$\frac{1}{M_A} \frac{\partial L}{\partial x_A} - \frac{1}{M_B} \frac{\partial L}{\partial x_B} = \frac{1}{M_A} \frac{d}{dt} \frac{\partial L}{\partial \mathbf{v}_A} - \frac{1}{M_B} \frac{d}{dt} \frac{\partial L}{\partial \mathbf{v}_B}. \quad (3.9)$$

After transforming to the center-of-mass (CM) frame using the relations in [65] and the identities (A3) and (A4) for derivatives of $(\partial_L r^{-1})^2$ and contractions of STF multilinear of unit vectors, we obtain

$$a_{rel,tid}^i = -G^2 \alpha^2 M \sum_{\ell} \frac{(2\ell - 1)!! (\ell + 1)}{r^{2\ell+3}} n^i \zeta_{\ell}, \quad (3.10)$$

in agreement with the known results in the limit $\lambda_S^{\ell}, \lambda_{ST}^{\ell} \rightarrow 0$. The nontidal part of the relative acceleration that adds to (3.10) to yield the total acceleration can be found in (B4).

C. Tidal contributions to the binding energy

Next, we compute the binding energy of the system from the Lagrangian (B1). Assuming a quasi-circular orbit $\dot{r} = \ddot{r} = 0$, we can express the binding energy in terms of the orbital frequency by using $\omega^2 = -\mathbf{a} \cdot \mathbf{r} / r^2$ instead of the coordinate dependent orbital radius parameter. The tidal contribution to this radius-frequency relationship is

$$\omega_{tid}^2 = \frac{G\alpha M}{r^3} \left[\frac{\alpha M}{r} \left(\sum_{\ell} \frac{(\ell + 1)(2\ell - 1)!!}{r^{2\ell} M} \zeta_{\ell} \right) \right]. \quad (3.11)$$

The full expression including also the point-mass terms is given in (B5). Inverting this expression results in (B6) with tidal contribution

$$r(x)_{tid} = \frac{G\alpha M}{x} \left[-\frac{1}{3} x \left(\sum_{\ell} \frac{(2\ell - 1)!! (\ell + 1)}{G^{2\ell} \alpha^{2\ell} M^{1+2\ell}} x^{2\ell} \zeta_{\ell} \right) \right], \quad (3.12)$$

where we introduce the frequency parameter

$$x = (G\alpha M \omega)^{2/3}. \quad (3.13)$$

Analogously to [49], we then obtain the tidal contribution to the binding energy

$$E_{tid}(x) = -\frac{\mu x}{2} \left[-\frac{1}{3} \sum_{\ell} (2\ell - 1)!! (4\ell + 1) \frac{G^{-2\ell} \zeta_{\ell}}{M^{2\ell+1} \alpha^{2\ell}} x^{2\ell+1} \right], \quad (3.14)$$

in agreement with the dipolar expression in [49], and the generic multipolar order result in [76]. The complete result for the binding energy including also the point-mass terms is given in (B7).

IV. TIDAL EFFECTS IN THE SCALAR AND GRAVITATIONAL RADIATION

The gravitational waveforms generated by the dynamics of the binary computed in the previous section can be constructed from the radiative solution of the field equations (2.18), (2.23) in the far zone. The field equations can be written as wave equations when introducing the gothic metric $\mathfrak{g}^{ab} = \sqrt{-g}g^{ab}$ [75] and expanding this metric and the scalar field around Minkowski spacetime and the scalar field background respectively. In the harmonic gauge $\partial_\nu \mathfrak{g}^{\mu\nu} = 0$ this results in

$$\begin{aligned} \square_\eta h^{\alpha\beta} &= \frac{1}{16\pi G} \mu^{\alpha\beta}, \\ \mu^{\alpha\beta} &= (-g)T_m^{\alpha\beta} + 16\pi G (\Lambda^{\alpha\beta}) \\ \Lambda^{\alpha\beta} &= 16\pi G (-g)t_{LL}^{\alpha\beta} + h_{,\mu}^{\alpha\nu} h_{,\nu}^{\beta\mu} - h^{\mu\nu} h_{,\mu\nu}^{\alpha\beta}, \end{aligned} \quad (4.1)$$

where $t_{LL}^{\alpha\beta}$ is the Landau-Lifshitz energy momentum pseudo tensor [77]. The scalar field equation of motion, with $\varphi = \varphi_0 + \delta\varphi$ and $\delta\varphi$ capturing the scalar waveform, is given by

$$\begin{aligned} \square_\eta \delta\varphi &= 4\pi G \mu_s \\ \mu_s &= -\frac{1}{\sqrt{-g}} \frac{\delta S_m}{\delta\varphi}. \end{aligned} \quad (4.2)$$

We can write these fields as integrals over the past lightcone by using the retarded Greens function

$$\begin{aligned} h^{\alpha\beta}(t, \mathbf{x}) &= -4G \int d^4x' \frac{\mu^{\alpha\beta}(t', \mathbf{x}') \delta(t' - t + |\mathbf{x} - \mathbf{x}'|)}{|\mathbf{x} - \mathbf{x}'|}, \\ \delta\varphi(\mathbf{x}) &= -G \int d^4x' \frac{\mu_s(t', \mathbf{x}') \delta(t' - t + |\mathbf{x} - \mathbf{x}'|)}{|\mathbf{x} - \mathbf{x}'|}. \end{aligned} \quad (4.3)$$

For the solutions to 1PN order we are considering, the direct integration approach of [73, 78, 79] applies. We split the integration domain of (4.3) over the past lightcone into the part that lies in the near zone and the part in the far zone. As shown in [63, 73, 75, 78], the far zone contributions are higher than 1PN order. As in the far zone contribution to the integral there are no matter sources, the contribution needs to come from back reaction effects which are generally higher order. For the details on performing these integrals we refer to [63–65, 67, 75]. Below, we discuss the tidal contributions to the waveforms.

A. Tidal contributions to the scalar waveform

In the near zone we expand (4.3) in the following multipole expansion based on the fact that far from the source $x'/|\mathbf{x} - \mathbf{x}'| = x'/d \ll 1$ to obtain

$$\begin{aligned} \delta\varphi(\mathbf{x}) &= \sum_{l=0}^{\infty} \delta\varphi_\ell(\mathbf{x}) \\ &= -G \sum_{l=0}^{\infty} \frac{(-1)^\ell}{\ell!} \partial_L \left(\frac{1}{d} I_s^L(\tau) \right), \end{aligned} \quad (4.4)$$

where the scalar radiative multipole moments are given by

$$I_s^L = I_s^L|_{\text{pp}} + Q_S^L, \quad (4.5)$$

where the point-particle (pp) contribution is

$$I_s^L(\tau)|_{\text{pp}} = \int_{\mathcal{M}} d^3x' \mu_s(\tau, \mathbf{x}') \mathbf{x}'^L. \quad (4.6)$$

Here, we introduced the retarded time $\tau = t - d$ and the hypersurface \mathcal{M} cut out by the intersection of the near zone with the constant time hypersurface $t_{\mathcal{M}} = \tau$. As the region \mathcal{M} is bounded, the integral is convergent. For the tidal contribution we use (2.15a) and (3.4a), (3.4b) and convert to the center-of-mass frame using the expressions from [65] to obtain

$$Q_L^S = G \frac{(-1)^\ell r_{<L>} (2\ell - 1)!!}{r^{2\ell+1}} \bar{\zeta}_\ell. \quad (4.7)$$

here we redefined $r_{<L>} = r_{<L>}^A$ and the two body dependencies are captured in the tidal coefficient

$$\begin{aligned} \bar{\zeta}_\ell &= -M_A q_A \lambda_{S,B}^\ell - M_B q_B (-1)^\ell \lambda_{S,A}^\ell \\ &\quad + M_A \lambda_{ST,B}^\ell + M_B (-1)^\ell \lambda_{ST,A}^\ell, \end{aligned} \quad (4.8)$$

the factor $(-1)^\ell$ arises from $r_{<L>}^B = (-1)^\ell r_{<L>}^A$. We are interested in radiation near future null infinity, where d is very large. Thus, when derivatives in (4.4) act on $1/d$ they will give strongly suppressed contributions which we neglect. To compute derivatives of the multipole moments we use that

$$\partial_i I_s(\tau) = \frac{\partial\tau}{\partial x^i} \frac{dI_s}{d\tau} = -N^i \frac{dI_s}{d\tau} = -N^i \frac{dI_s}{dt}, \quad (4.9)$$

where $\mathbf{N} = (\mathbf{x} - \mathbf{x}')/d$ is a unit vector pointing from the source to the field point. Thus, the multipolar scalar waves near null infinity are given by

$$\delta\varphi_\ell(\mathbf{x}) = \frac{G N_L}{d \ell!} \left(\frac{\partial}{\partial t} \right)^\ell I_s^L + \mathcal{O}(d^{-2}). \quad (4.10)$$

From (4.5) it follows that the scalar waveform consist of the point-particle and linear tidal contributions. We express the latter more explicitly by rewriting time derivatives of the tidal multipoles (4.7) using the generalized Leibniz rule

$$\left(\frac{\partial}{\partial t} \right)^\ell r^{-(2\ell+1)} r_{<L>} = \sum_{k=0}^{\ell} \binom{\ell}{k} \partial_t^{\ell-k} r_{<L>} \partial_t^k r^{-(2\ell+1)}. \quad (4.11)$$

This can be further manipulated using Faà di Bruno's formula [80]

$$\begin{aligned} \left(\frac{\partial}{\partial t} \right)^\ell r^{-(2\ell+1)} r_{<L>} &= \sum_{k=0}^{\ell} \frac{\ell!}{k! (\ell - k)!} \partial_t^{\ell-k} r_{<L>} \times \\ &\quad \sum_{p=1}^k \frac{(2\ell + p)! (-1)^p}{(2\ell)! r^{2\ell+p+1}} B_{k,p}(\dot{r}, \ddot{r}, \dots, r^{k-p+1}), \end{aligned} \quad (4.12)$$

with $B_{k,p}$ the incomplete Bell polynomials. Using this, the total tidal contribution to the scalar waveform can be written as

$$\delta\varphi_{tid} = \sum_{\ell} \sum_{k=0}^{\ell} \sum_{p=1}^k \frac{G^2 N^L \bar{\zeta}_{\ell} (2\ell+p)! (-1)^{p+\ell}}{d k! (\ell-k)! 2^{\ell}} \times \frac{\partial_t^{\ell-k} r_{<L>}}{r^{2\ell+p+1}} B_{k,p}(\dot{r}, \ddot{r}, \dots, r^{k-p+1}). \quad (4.13)$$

For the total 1PN scalar waveform with tidal corrections see (B7).

B. Tidal contributions to the tensor waveform

Similar to the scalar waveform, the near-zone contributions to the tensor radiation fields can be expressed as a multipole expansion, though some differences arise because the source term of the field equation is a tensor, as explained in Sec. C of [78]. This leads to the radiative fields

$$h^{ij}(t, \mathbf{x}) = \frac{2G}{d} \sum_{\ell=0}^{\infty} \frac{1}{\ell!} N_{L-2} \left(\frac{\partial}{\partial t} \right)^{\ell} I^{ij L-2} + O(d^{-2}), \quad (4.14)$$

where $I^{ij L-2}$ are the tensor radiative multipole moments given by

$$I^{ij L-2} = I^{ij L-2} |_{\text{EW}} + Q_T^{ij L-2}. \quad (4.15)$$

Here, the first term are related to the Epstein-Wagoner multipole moments for point masses [81] and the second one the tidal multipoles (2.15b). From (2.15b) and (3.4a), (3.4b) we obtain, after converting to the center-of-mass frame using the expressions from [65] and proceeding as in (4.13),

$$Q_L^T = G \frac{(-1)^{\ell} r_{<L>} (2\ell-1)!!}{r^{2\ell+1}} \tilde{\zeta}_{\ell}, \quad (4.16)$$

with

$$\tilde{\zeta}_{\ell} = -M_A q_A \lambda_{ST,B}^{\ell} - M_B q_B (-1)^{\ell} \lambda_{ST,A}^{\ell} + M_A \lambda_{T,B}^{\ell} + M_B (-1)^{\ell} \lambda_{T,A}^{\ell}.$$

Using (4.11), (4.12) we obtain for the direct tidal contribution to the tensor waveform

$$h_{Q^T}^{ij} = \sum_{\ell=2} \sum_{k=0}^{\ell} \sum_{p=1}^k \frac{4G^2 N^{L-2} \tilde{\zeta}_{\ell} (2\ell+p)! (-1)^{p+\ell}}{d k! (\ell-k)! 2^{\ell}} \times \frac{\partial_t^{\ell-k} r_{<L>}}{r^{2\ell+p+1}} B_{k,p}(\dot{r}, \ddot{r}, \dots, r^{k-p+1}). \quad (4.17)$$

Additionally, the time derivatives in (4.14) acting on the point mass multipoles in (4.15) introduce tidal contributions coming from the relative acceleration (3.10). These involve terms proportional to the parameter ζ_{ℓ} defined

in (3.8). Together with this contribution, the tidal terms in the tensor waveform read

$$h_{tid}^{ij} = - \sum_{\ell} \frac{4G^3 \mu \alpha^2 M^2 (1+\ell) (2\ell-1)!! \zeta_{\ell}}{d r^{2(2+\ell)}} r^i r^j + \sum_{\ell=2} \sum_{k=0}^{\ell} \sum_{p=1}^k \frac{4G^2 N^{L-2} \tilde{\zeta}_{\ell} (2\ell+p)! (-1)^{p+\ell}}{d k! (\ell-k)! 2^{\ell}} \times \frac{\partial_t^{\ell-k} r_{<L>}}{r^{2\ell+p+1}} B_{k,p}(\dot{r}, \ddot{r}, \dots, r^{k-p+1}). \quad (4.18)$$

For the full 1PN tensor waveform see (B9).

Using the standard convention [78] of an orthonormal triad composed of the vectors \mathbf{N} in the radial direction of the observer, $\hat{\mathbf{p}}$ along the intersection of the orbital plane with the sky and $\hat{\mathbf{q}} = \mathbf{N} \times \hat{\mathbf{p}}$, the plus and cross polarizations of the waveform are given by

$$h_+ = \frac{1}{2} (\hat{p}_i \hat{p}_j - \hat{q}_i \hat{q}_j) h^{ij}, \quad (4.19)$$

$$h_{\times} = \frac{1}{2} (\hat{p}_i \hat{q}_j + \hat{q}_i \hat{p}_j) h^{ij}.$$

For contracting the vectors, we use the identities given in [78] but do not write out the explicit results here.

C. Gravitational waves in the Jordan frame

The scalar and gravitational radiation computed in Sec. IV were based on the Einstein-frame formulation of the ST theory, as discussed in Sec. II E. Here, we review the transformation of these results to the Jordan frame. The fact that the matter sector of the Jordan-frame formulation of ST theories is the standard model of particle physics implies that one can use existing results for how a GW detector measures signals in that frame. In Appendix D we provide the derivation of the results for the transformations and further discussion based on geodesic deviation and the frame transformation (2.2) and (2.4), generalizing the results of [63, 82, 83] to generic coupling functions. We obtain that the Jordan-frame waveform is given in terms of Einstein-frame quantities by

$$h_{ij}^{\text{Jordan}} \simeq h_{ij} + \frac{2A'(\varphi_{\infty})}{A(\varphi_{\infty})} \delta\varphi \delta_{ij}, \quad (4.20)$$

where h_{ij} is the waveform computed in Sec. IV B and given explicitly by (B9), and $\delta\varphi$ the scalar waveform computed in Sec. IV A and given explicitly in (B7). The approximation is that we work in a region of space-time asymptotically far from the binary source, where the scalar field is dominated by its constant asymptotic value φ_{∞} , and to linear order in small perturbations around an asymptotic background, both for the metric and scalar fields. Applying the decomposition into the tensorial plus and cross polarizations (4.19) to (4.20) and using the orthonormality of the spatial triad shows that the tensor polarization amplitudes in the Jordan frame

$h_{+/\times}^{\text{Jordan}} = h_{+/\times}$ coincide with those in the Einstein frame given in (4.19). In addition, the scalar contribution to the GWs in (4.20) gives rise to an extra scalar polarization component of the GWs. Depending on the coupling function and cosmological value of the scalar field, this contribution may, however, be suppressed by many orders of magnitude.

D. Energy fluxes

The gravitational and scalar radiation cause an energy flux out of the binary system proportional to the angular integral over the square of the time derivative of the waveforms. Similar to Sec. III C we are interested in the fluxes and phase evolution in terms of the coordinate independent orbital frequency for quasi circular orbits. We substitute (B6) in the waveforms (B7), (B9) and expand perturbatively to linear order in the tidal contributions. This requires explicitly evaluating $r_{<L>}$ in (4.13), (4.18). Hence from this section onward we consider only multipole moments up to $\ell = 2$, where all three different tidal contributions (S/T/ST) appear. Below we discuss these tidal contributions to the scalar and tensor energy fluxes.

1. Tidal contributions to the scalar energy flux

The scalar energy flux can be obtained from the scalar waveform via the surface integral

$$\mathcal{F}_S = \frac{d^2}{4\pi G} \oint \delta\dot{\varphi}^2 d^2\Omega. \quad (4.21)$$

We perform the angular integral over the products of unit vectors N_i using the identities from [69] and substitute (B7) to obtain

$$\begin{aligned} \mathcal{F}_{S,tid} = & \frac{4G^3 M S_- \alpha^{3/2} \mu}{3r^6} \left(9\dot{r} - 3v^2 + \frac{2GM\alpha}{r} \right) \bar{\zeta}_1 \\ & + \frac{8G^4 M^2 S_-^2 \alpha^4 \mu^2}{3r^7} \left(2\zeta_1 + 9\frac{\zeta_2}{r^2} \right), \end{aligned} \quad (4.22)$$

with

$$S_{\pm} \equiv \frac{q_A \pm q_B}{2\sqrt{\alpha}}, \quad (4.23)$$

and α , ζ_ℓ and $\bar{\zeta}_\ell$ defined in (3.7), (3.8) and (4.8) respectively. Assuming quasi-circular orbits, substituting (B6), and expressing the flux in terms of the frequency parameter x defined in (3.13), we obtain

$$\begin{aligned} \mathcal{F}_{S,tid} = & x^7 \left(-\frac{4S_- \mu \bar{\zeta}_1}{3\alpha^{9/2} G^3 M^5} + \frac{16S_-^2 \mu^2 \zeta_1}{9\alpha^3 G^3 M^5} \right) \\ & + x^9 \frac{S_-^2 \mu^2 \zeta_2}{\alpha^5 G^5 M^7}. \end{aligned} \quad (4.24)$$

In the expressions above two types of tidal contributions arise. The $\bar{\zeta}_1$ term results from (4.13) due to the induced tidal moments. We find that only the odd ℓ give a nontrivial contribution to the integral. The $\zeta_{\ell=1,2}$ terms come in via the relative acceleration contributions (3.10) which arise from the time derivative to the waveform. The full 1PN scalar flux for the point-mass part is given by (B10) and (B11).

2. Tidal contribution to the tensor energy flux

The tensor energy flux is constructed via

$$\mathcal{F}_T = \frac{d^2}{32\pi G} \oint \dot{h}_{\text{TT}}^{ij} \dot{h}_{\text{TT}}^{ij} d^2\Omega, \quad (4.25)$$

where TT denotes the transverse-traceless piece obtained with the aid of the projection operator

$$P^{ij} = \delta^{ij} - N^i N^j \quad (4.26)$$

to reduce to the transverse part and removing all traces. Note that the derivatives to the tensor waveforms are taken in the TT gauge². The angular integral is again computed using the identities in [69]. Substituting the explicit expression for the tensor waveform (B9) into (4.25) we find the following expression for the tidal contributions to the tensor flux

$$\begin{aligned} \mathcal{F}_{T,tid} = & \frac{48G^3 M \alpha \mu}{5r^8} \left(100\dot{r}^4 - 105\dot{r}^2 v^2 + 15v^4 \right. \\ & + 18 \frac{GM\alpha}{r} \dot{r}^2 - 11 \frac{GM\alpha}{r} v^2 \left. \right) \tilde{\zeta}_2 \\ & - \frac{64G^4 M^2 \alpha^3 \mu^2}{15r^7} (7\dot{r}^2 - 6v^2) \zeta_1 \\ & - \frac{192G^4 M^2 \alpha^3 \mu^2}{5r^9} (4\dot{r}^2 - 3v^2) \zeta_2 \end{aligned} \quad (4.27)$$

with ζ_ℓ and $\tilde{\zeta}_\ell$ defined in (3.8) and (4.17). Again assuming quasi-circular orbits and expressing the flux in terms of the frequency, we obtain

$$\begin{aligned} \mathcal{F}_{T,tid} = & x^8 \frac{256\mu^2 \zeta_1}{15\alpha^4 G^3 M^5} \\ & + x^{10} \left(\frac{192\mu \tilde{\zeta}_2}{5\alpha^7 G^5 M^7} + \frac{384\mu^2 \zeta_2}{5\alpha^6 G^5 M^7} \right). \end{aligned} \quad (4.28)$$

Similar to the scalar flux we find again two types of tidal contributions. The $\tilde{\zeta}_2$ term results from (4.18) due to the

² Using the definition of the projector operator one can use the identity $(P^{ik} P^{jl} - \frac{1}{2} P^{ij} P^{kl}) (P^{im} P^{jn} - \frac{1}{2} P^{ij} P^{mn}) = P^{km} P^{ln} - \frac{1}{2} P^{kl} P^{mn}$ to simplify the integral (4.25) to $\mathcal{F}_T = \frac{\mu^2}{32\pi G} \oint \left(4\dot{Q}^{ij} \dot{Q}^{ij} - 8N^{ln} \dot{Q}^{kl} \dot{Q}^{kn} + 2N^{klmn} \dot{Q}^{kl} \dot{Q}^{mn} \right) d^2\Omega$. Here Q is defined as $Q_{ij} = \tilde{Q}_{ij} - \frac{1}{3} \delta_{ij} \tilde{Q}_k^k$ with $\tilde{Q}_{ij} = \frac{d}{2G\mu} h_{ij}$.

induced tidal moments. Now only the even ℓ contribute to the integral. The $\zeta_{\ell=1,2}$ terms come in via the relative acceleration. For the 1PN tensor flux see (B13) and (B14). Together with the scalar flux in (B10) the total flux is the sum of the two contributions $\mathcal{F} = \mathcal{F}_S + \mathcal{F}_T$.

E. GW phase evolution

During the quasi-circular inspiral, the corrections to the radiation compared to the radiation in GR are accumulated over many GW cycles in the phase evolution. In this regime, the motion is approximately adiabatic, with $\dot{\omega}/\omega^2 \ll 1$ and there is an energy balance between the binding energy of the system and the radiative energy flux $\dot{E}(\omega) = -\mathcal{F}(\omega)$. Together with the change in orbital phase $\dot{\phi} = \omega$ this gives the system of differential equations

$$\frac{d\phi}{dt} - \omega = 0, \quad \frac{d\omega}{dt} + \frac{\mathcal{F}(\omega)}{E'(\omega)} = 0. \quad (4.29)$$

As the results for $E(x)$ and $\mathcal{F}(x)$ are only available perturbatively, there are different choices for how to solve (4.29), as reviewed e.g. in [84]. With regard to data analysis it is useful to obtain the expressions for the phase evolution in the Fourier domain. The Fourier transform of the gravitational strain measured by a detector and denoted by \tilde{h} can be obtained using the stationary phase approximation (SPA) [85]

$$\tilde{h}^{\text{SPA}}(f) = \mathcal{A} \sqrt{\frac{2\pi}{M\dot{\omega}}} e^{-i[\psi(f) + \pi/4]}, \quad (4.30)$$

with \mathcal{A} the amplitude and $\psi \equiv 2\phi(t(f)) - 2\pi ft(f)$ the Fourier phase. One can rewrite (4.29) as a second order differential equation in terms of the Fourier phase

$$\frac{d^2\psi(\omega)}{d\omega^2} = -2 \frac{E'(\omega)}{\mathcal{F}(\omega)}. \quad (4.31)$$

Using (3.13) this leads to

$$\psi = - \int \left(\int \frac{E'(x)}{\mathcal{F}(x)} dx \right) \frac{3\sqrt{x}}{G\alpha M} dx + \phi_c - 2\pi ft_c, \quad (4.32)$$

where ϕ_c , t_c are integration constants determined by the choice of reference point in the evolution. To solve (4.32) we use the Taylor F2 approximant [84], where the integrand is expanded perturbatively in x and in tidal corrections using the explicit expressions for the fluxes (B11), (B14) and binding energy (B7). The presence of both scalar and gravitational radiation in the system leads to different behaviors depending on the frequency regime: for small frequencies, the scalar dipole terms in the total flux (proportional to x^4 in (B11)) are dominant, while for larger frequencies the tensor quadrupole terms (proportional to x^5 in (B14)) become the dominant contributions. These regimes are

commonly referred to as the dipolar driven (DD) and quadrupolar driven (QD) regimes respectively. Specifically, based on the leading order contributions to the flux, the regime for which the scalar dipole dominates is

$$x^{\text{DD}} \ll \frac{5\mathcal{S}_-^2\alpha}{24} \text{ or } f^{\text{DD}} \ll \left(\frac{5}{24}\right)^{3/2} \frac{\mathcal{S}_-\sqrt{\alpha}}{\pi GM}, \quad (4.33)$$

see [49] for a study of the validity of this approximation to the transition frequency between the two regimes.

1. Phase evolution in the Dipolar-Driven domain

For frequencies in the regime denoted by (4.33) the dipolar term in the total flux is leading. We factor out this term and expand the ratio up to 1PN, which gives the following form

$$\frac{E'(x)}{\mathcal{F}^{\text{DD}}(x)} = \frac{-3\alpha GM}{8\eta\mathcal{S}_-^2x^4} [1 + (E'_0 - f_2^{\text{DD}})x], \quad (4.34)$$

with the symmetric mass ratio

$$\eta = \frac{\mu}{M} \quad (4.35)$$

and the coefficient f_2^{DD} given by (B16). Substituting (4.34) in (4.32) gives the following result for the Fourier phase angle in the DD domain (B17), where we show only the tidal contributions here

$$\psi_{\text{tid}}^{\text{DD}} = \frac{1}{4\eta\mathcal{S}_-^2x^{3/2}} \left\{ x^3 \left[\rho_{\text{tid}}^{\text{DD}} \log(x) - \frac{2}{3}\rho_{\text{tid}}^{\text{DD}} \right] - \frac{270\zeta_2}{7\alpha^4G^4M^5}x^5 \right\} + \phi_c - 2\pi ft_c, \quad (4.36)$$

with

$$\rho_{\text{tid}}^{\text{DD}} = \frac{3}{G^2\alpha^2M^3\eta} \left(-\frac{\bar{\zeta}_1}{\alpha^{3/2}MS_-} + 16\eta\zeta_1 \right). \quad (4.37)$$

The total phase including also the point-mass terms is given in (B17). Looking at the prefactor of (4.36) we see that the phase angle diverges for $S_- \rightarrow 0$, where S_- was defined in (4.23). This parameter vanishes for an equal mass system where both bodies have the same scalar charge q . However, as the scalar flux terms are proportional to S_- the scalar radiation, and therefore the DD regime, vanishes for these systems and the expansion used to obtain ψ_{DD} which assumed the scalar flux is leading is invalid and would need to be modified.

2. Phase evolution in the Quadrupolar-Driven domain

For frequencies above (4.33) the quadrupolar contribution in the total flux is leading. We split the total flux in its scalar and tensor contributions and factor the dipolar and quadrupolar term labelling them non-dipolar and

dipolar respectively. This leads to $\mathcal{F} = \mathcal{F}_{\text{non-dip}} + \mathcal{F}_{\text{dip}}$ with

$$\begin{aligned}\mathcal{F}_{\text{non-dip}} &= \frac{32\eta^2\xi}{5G\alpha^2}x^5(1+f_2^{nd}x), \\ \mathcal{F}_{\text{dip}} &= \frac{4\mathcal{S}_-^2\eta^2}{3G\alpha}x^4(1+f_2^dx),\end{aligned}\quad (4.38)$$

where

$$\xi = 1 + \mathcal{S}_+^2\alpha/6, \quad (4.39)$$

and the other coefficients given in (B21). We then expand the ratio in (4.32) as

$$\frac{E'(x)}{\mathcal{F}(x)} \simeq \frac{E'(x)}{\mathcal{F}_{\text{non-dip}}(x)} \left(1 - \frac{\mathcal{F}_{\text{dip}}(x)}{\mathcal{F}_{\text{non-dip}}(x)}\right), \quad (4.40)$$

which results in

$$\begin{aligned}\frac{E'(x)}{\mathcal{F}(x)} &\simeq -\frac{5GM\alpha^2}{64\eta\xi x^5} [1 + (E'_0 - f_2^{nd})x] \\ &+ \frac{25GM\alpha^3\mathcal{S}_-^2}{1536\xi^2\eta x^5} [1 + (E'_0 - 2f_2^{nd} + f^d)x].\end{aligned}\quad (4.41)$$

Substituting (4.41) in (4.32) gives the Fourier phase in the QD domain (B22), with the tidal contributions

$$\psi^{\text{QD}} = \psi_{\text{non-dip}} + \psi_{\text{dip}} + \phi_c + 2\pi ft_c, \quad (4.42)$$

with

$$\psi_{\text{non-dip,tid}} = \frac{3\alpha}{128\eta\xi x^{5/2}} \left[\rho_{\text{tid}}^{nd,1}x^3 + \rho_{\text{tid}}^{nd,2}x^5 \right], \quad (4.43a)$$

$$\begin{aligned}\psi_{\text{dip,tid}} &= -\frac{5\mathcal{S}_-^2\alpha^2}{1792\eta\xi^2x^{7/2}} \left[\rho_{\text{tid}}^{d,1}x^3 + \rho_{\text{tid}}^{d,2}x^5 \log(x) \right. \\ &\quad \left. - \frac{2}{3}\rho_{\text{tid}}^{d,2}x^5 \right],\end{aligned}\quad (4.43b)$$

The non-dipolar tidal coefficients are given by

$$\rho_{\text{tid}}^{nd,1} = \frac{400\zeta_1}{3\alpha^2G^2M^3} + \frac{160\zeta_1}{3\alpha^2G^2M^3\xi}, \quad (4.43c)$$

$$\rho_{\text{tid}}^{nd,2} = -\frac{24\tilde{\zeta}_2}{\alpha^5G^4M^6\xi\eta} - \frac{216\zeta_2}{\alpha^4G^4M^5} - \frac{48\zeta_2}{\alpha^4G^4M^5\xi}, \quad (4.43d)$$

and the dipolar parts are

$$\begin{aligned}\rho_{\text{tid}}^{d,1} &= -\frac{35\bar{\zeta}_1}{2\alpha^{7/2}G^2M^4S_- \eta} - \frac{280\zeta_1}{3\alpha^2G^2M^3} \\ &\quad - \frac{280\zeta_1}{3\alpha^2G^2M^3\xi},\end{aligned}\quad (4.43e)$$

$$\rho_{\text{tid}}^{d,2} = -\frac{140\tilde{\zeta}_2}{\alpha^5G^4M^6\eta\xi} - \frac{560\zeta_2}{\alpha^4G^4M^5} - \frac{280\zeta_2}{\alpha^4G^4M^5\xi}. \quad (4.43f)$$

3. Expressions for the tidal phasing in ready-to-use form

The tidal phase contributions (4.43) can be expressed as

$$\begin{aligned}\psi_{\text{tid}}^{\text{QD}} &= \frac{3}{128\eta x^{5/2}} [c_2S_-x^2 + c_3x^3 \\ &\quad + c_4S_-^2 \left(\log x - \frac{2}{3} \right) x^4 + \left(\frac{39}{2\alpha^5\xi^2}\tilde{\Lambda} + c_5 \right) x^5],\end{aligned}\quad (4.44)$$

where the various coefficients c_i for $i = 2, 3, 4, 5$ are given explicitly in terms of masses, scalar charges, and tidal deformabilities of the bodies in (C1)–(C4) in appendix C1 and α and ξ were defined in (3.7) and (4.39), with S_\pm given in (4.23) and x defined in (3.13), which includes a dependence on α . We have also introduced the parameter $\tilde{\Lambda}$ having the same functional form as in GR and involving the quadrupolar tensor deformabilities [42, 86]

$$\tilde{\Lambda} = \frac{16}{13M^5G^4} \left[(11M_B + M) \frac{\lambda_A^T}{M_A} + (11M_A + M) \frac{\lambda_B^T}{M_B} \right], \quad (4.45)$$

however, as λ^T are computed within ST gravity, $\tilde{\Lambda}$ may differ from its value in GR.

The coefficients c_2 and c_3 in (4.44) depend only on scalar dipolar tidal effects, while c_4 and c_5 involve all quadrupolar tidal parameters. Moreover, for the case of identical NSs, S_- defined in (4.23) vanishes and hence the effects encapsulated in c_2 and c_4 do not contribute in that case. The remaining coefficients for identical masses m , scalar charges q , and tidal deformabilities λ_ℓ are given by

$$c_3|_{A=B} = \frac{1680q^2(1 + \frac{5}{42}q^2)}{(1+q^2)^5(6+q^2)^2} \Lambda_1^S, \quad (4.46)$$

$$\begin{aligned}c_5|_{A=B} &= \frac{702}{(1+q^2)^5(6+q^2)^2} \left[\frac{7}{26}q^2\Lambda_2^T \right. \\ &\quad \left. + \frac{q(26+5q^2)}{26}\Lambda_2^{ST} - \frac{q(22+3q^2)}{26}\Lambda_2^S \right].\end{aligned}\quad (4.47)$$

Here, we have defined the dimensionless deformabilities

$$\Lambda_\ell = \frac{\lambda_\ell}{G^{2\ell}m^{2\ell+1}}. \quad (4.48)$$

We also note that for the case of identical NSs, $\tilde{\Lambda} = \Lambda_2^T$ and $\alpha^5\xi^2 = (1+q^2)^5(6+q^2)^2/36$. Finally, we see that in the case of GR, where $S_- = c_3 = c_5 = 0$ and $\alpha = \xi = 1$ we recover the standard result for the leading-order quadrupolar tidal effects [42, 86].

V. CASE STUDY OF NEUTRON STAR BINARIES

A. Set-up and properties of single neutron stars

We next apply the general results of the previous section to NS binary and BH-NS systems in specific classes

of ST theories.

1. Choice of coupling

We consider ST theories characterized by the Damour-Esposito-Farèse coupling [20],

$$A(\varphi) = e^{\frac{1}{2}\beta_0\varphi^2}. \quad (5.1)$$

These theories contain two arbitrary parameters; the above entered β_0 and φ_∞ , the value of the scalar field at spatial infinity. One can rewrite these free quantities by the following parameters

$$\alpha_0 = \alpha(\varphi_\infty) = \partial \ln A(\varphi_\infty) / \partial \varphi_\infty = \beta_0 \varphi_\infty, \quad (5.2)$$

capturing the strength of the coupling between the scalar field to matter in the asymptotic limit and its derivative

$$\beta_0 = \partial \alpha(\varphi_\infty) / \partial \varphi_\infty, \quad (5.3)$$

as solar system test probe directly α_0 or combined parameters of α_0 and β_0 [19, 20, 28]. When β_0 is sufficiently negative, $\beta_0 \lesssim -4.3$ [22], NS solutions become scalarized. That is, in these cases NSs are not only described by the mass and EoS relating the pressure and density, but also by the properties of the scalar field. This threshold value of β_0 is largely insensitive to the choice of α_0 , which for increasing $|\alpha_0|$ mostly smooths the sudden scalarization effect [15, 24], leading to scalarized NSs over the whole mass range. For our case studies we adopt the choice of a cosmological background scalar field $\varphi_\infty = 10^{-3}$ and $\beta_0 = (-4.5, -6)$ corresponding to scalarized NS solutions, hence $|\alpha_0|$ is of order 10^{-3} . This corresponds to the upperbound value on this parameter from solar system tests of the Cassini spacecraft [28, 87, 88]. We do note that this $|\alpha_0|$ and $\beta_0 = -4.5$ are on the lower bound of being consistent with recent binary pulsar tests [24, 27–29]. This does depend on the choice of EoS, where softer EoS allow for a more negative lower bound on β_0 [28], however $\beta_0 = -6$ can be stated to be ruled out by current observations, regardless of the EoS [29]. Our main goal with these choices for β_0 is to show the effect and dependencies of this parameter on the tidal contributions to the waveforms for scalarized NSs. For more negative choices of β_0 the scalarization effects are enhanced and our choices for this parameter are therefore useful for a qualitative study of the parametric dependence. However we highlight that the case studies for $\beta_0 = -4.5$ show the more realistic results.

2. Properties of isolated and tidally perturbed NSs

For the numerical implementation to compute properties of NSs, we use the results from [45], which we briefly summarize.

The properties of NSs are obtained from the field equations derived from (2.1) with the matter action corresponding to a perfect-fluid energy-momentum tensor for a NS, together with stress-energy conservation. To solve the system requires specifying an EoS, for which we use a parameterized piecewise polytropic approximation to tabulated models [89] known as WFF1, SLy and H4. These EoS cover a range of possibilities from softer to stiffer EoSs that, for a given NS mass, lead a corresponding range of more or less compact stars respectively. To compute these properties we solve the equations of motion numerically using a shooting method, as described in [45]. Specializing the computations to an equilibrium configuration yields the mass, radius, and scalar charge of the NS. The upper panels of Fig. 3 show the results for the scalar charge for $\beta_0 = -4.5$ in the left panel and $\beta_0 = -6$ in the right panel. Each point corresponds to a different central density of the NS that increases from left to right along each curve. The steep rise in charge seen above a certain mass indicates the formation of a significant scalar condensate, i.e. the scalarization of the NS which occurs above a critical compactness, which is reached for lower masses in the case of softer EoSs. We further consider linear, static perturbations to this equilibrium configuration, which enables us to solve for the various tidal deformability parameters shown in the lower panels of Fig. 3 for a fixed intermediate SLy EoS. Here, the $\ell = 2$ scalar (S) and scalar-tensor (ST) values are rescaled by an order of magnitude as they would otherwise be too small to be visible on the plot, and in addition, the sign of the ST results is reversed. We see that in the case of $\beta_0 = -4.5$ (lower left panel), the tensor deformability (blue curves) is identical to its value in GR (dashed lines) for most of the mass range and only differs slightly for masses corresponding to a large scalarization. All other deformability parameters are much smaller than the tensor one throughout the mass range and also exhibit a significant enhancement for large scalarization. For larger values of β_0 (lower right panel), all effects of scalarization and scalar tides are larger, with all Love numbers attaining the same order of magnitude, however, the quadrupole tensor deformability also dominates over the others in most of the mass range.

B. Computation of $\beta(\varphi)$

To compute the skeletonized mass (3.2) requires not only information on the scalar charge, but also how it varies with the cosmological value of the scalar field, as parameterized by β in (3.2). This quantity was not computed in [45]. For objects with negligible self-gravity one can use that [18] $\beta = (d^2 \log A / d\varphi^2)_\infty$, where the evaluation is at the value of the scalar field at infinity. However, compact objects such as NSs have strong self-gravity and this formula does not apply. Thus, we compute β numerically by calculating the scalar charge q for a wide range of asymptotic scalar field values, interpolating the results

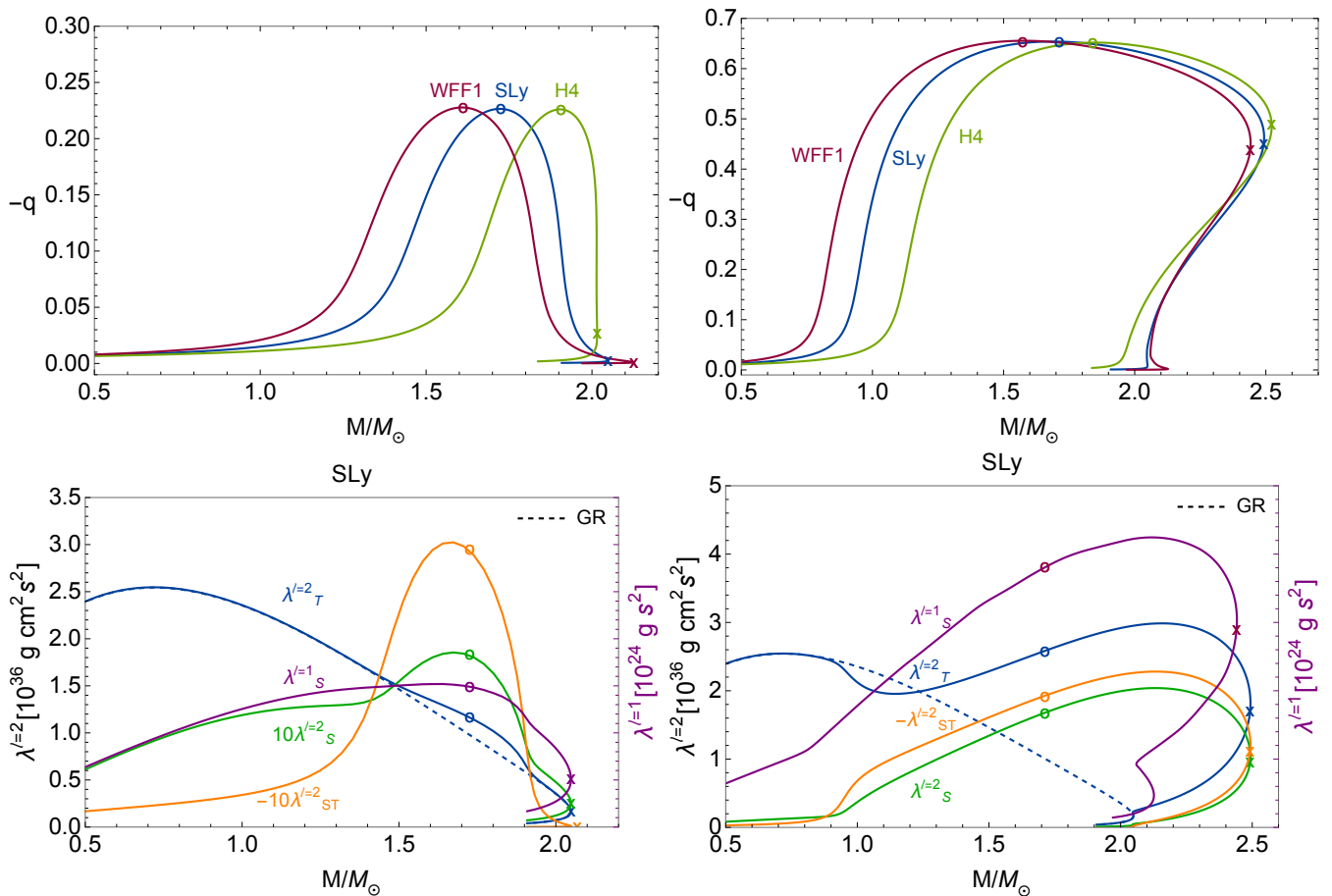


FIG. 3. Charge-mass curves (top row), and tidal deformabilities (bottom row) in the Einstein frame for three equations of state (WFF1, SLy, and H4). Quantities are shown for $\beta_0 = -4.5$ (left column) and $\beta_0 = -6$ (right column). Dashed lines represent the GR configurations $\beta_0 = 0$. In the bottom panels we fix the SLy EoS and show the different tidal deformabilities. We note the rescalings of some of the curves in the lower left panel and the different units of the dipolar scalar deformabilities (purple curves and right axes) and the quadrupolar ones (all other curves and left axes). Circles represent the maximum charge configuration, M_q , and crosses indicate the maximum mass.

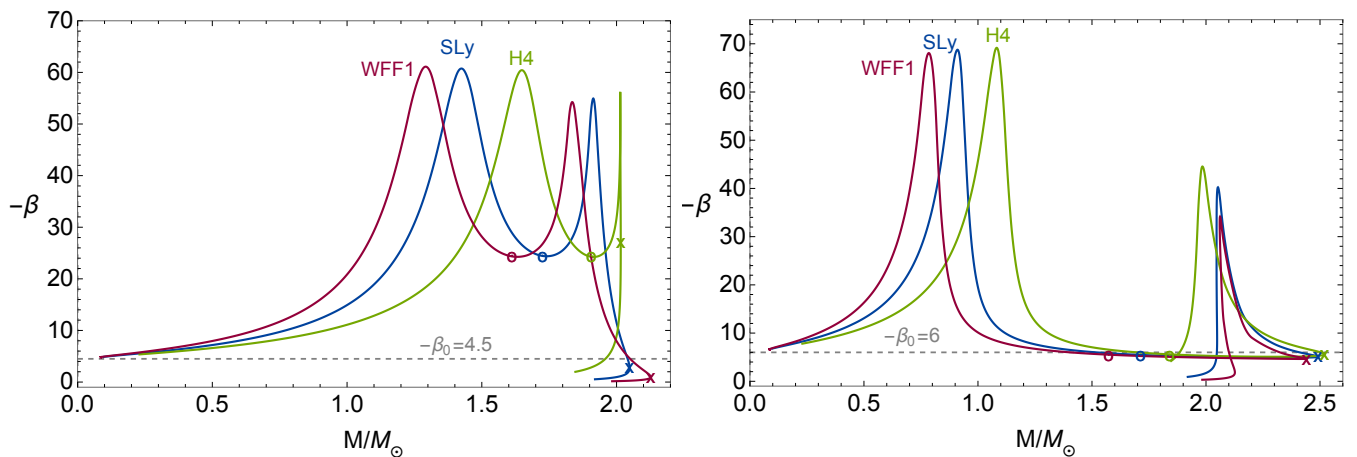


FIG. 4. Results for the parameter β characterizing the variation of the scalar charge with the field at its cosmological value as a function of mass. The results are computed in the Einstein frame for three EoS (WFF1, SLy, and H4) and for $\beta_0 = -4.5$ (left column) and $\beta_0 = -6$ (right column) for cosmological scalar field values of $\varphi_\infty = 10^{-3}$. Dashed lines represent the values of the coupling coefficient β_0 , circles indicate the maximum-charge configuration M_q , and crosses the maximum mass.

to obtain an approximate functional dependence on the field, and computing the numerical derivative of this interpolating function. Our implementation is based on an extension of the publicly available `Mathematica` code of [45, 90], which we use to generate data around the value of the desired cosmological scalar field $\varphi_\infty = 10^{-3}$. We compute results for $\varphi_\infty = [0.9, 1.1] \times 10^{-3}$ in increments of 0.01×10^{-3} . We then interpolate the data-points and differentiate the interpolation function to obtain β from (3.2b) with $\varphi_0 = \varphi_\infty$. We also compare this to results obtained directly approximating the numerical derivative by

$$\beta(\varphi_\infty) \approx \frac{q(\varphi_\infty + \Delta\varphi_\infty) - q(\varphi_\infty)}{\Delta\varphi_\infty}, \quad (5.4)$$

with $\Delta\varphi_\infty$ an infinitesimal increment. We found that taking $\Delta\varphi_\infty = 0.01 \times 10^{-3}$ is sufficiently small to resolve the derivative, while larger increments of 0.05×10^{-3} led to inconsistencies. With this setting, we obtain excellent agreement between the methods, with a maximum fractional difference between the approximation to the numerical derivative and the interpolation of 0.37%. This is expected as the dependence of q on the scalar field is smooth. Fig. 4 shows the results for β using the approximation to the numerical derivative (5.4). As a check on our calculations, we also verified that for $M \rightarrow 0$ we recover the analytical results for negligible self-gravity. We see that as a function of the NS mass, the maximum $|\beta|$ occurs for relatively low masses and takes a low value for the maximum scalar charge configuration M_q . For $\beta_0 = -4.5$ shown in the left panel of Fig. 4, the value of $|\beta|$ for the M_q configuration is a local minimum, and rises to larger values for higher masses before rapidly decreasing and for softer EoSs (WFF1, SLy shown as the red and blue curves respectively) even dropping below $|\beta_0|$ near the maximum mass. By contrast, for the stiffer H4 EoS (green curve), $|\beta|$ peaks abruptly around the maximum mass and remains well above $|\beta_0|$. Such a behavior was also noticed in [91], p. 530, and in Figure 3 of [15]. The behavior of $|\beta|$ is different for $\beta_0 = -6$ shown in the right panel of Fig. 4. In that case, all EoSs lead to a maximum value at low masses, fall off below $|\beta_0|$ near the maximum mass, and attain a secondary local maximum for NSs with central densities just above the maximum mass configuration. We note that while for NSs in GR, the maximum mass usually correlates with the onset of a gravitational instability, this is a priori not necessarily the case for the ST configurations considered here. We leave the stability analysis and hence the question if the behavior of β beyond the maximum mass is of physical significance to future work.

C. Waveform and frequency evolution of example binary systems

To gain intuition on the impact of tidal effects on the waveforms, we first consider in Fig. 5 the plus polariza-

tion of the time-domain waveforms (B9) and (4.19) with the phase evolution computed from (4.29) for a BH-NS binary system with masses $(5, 1.7)M_\odot$ (top panel) and a NS-NS system with masses $(1, 1.7)M_\odot$ (middle panel). In addition, the bottom panel shows the corresponding frequency evolution for the NS-NS system. The scalar charge and tidal deformability parameters are taken from the results shown in Fig. 3 for the SLy EoS and $\beta_0 = -4.5$ for NSs and set to zero for BHs. As the PN approximation is not valid for frequencies close to merger we cut off the functions at a benchmark GW frequency of 500Hz^3 and show a snapshot of the waveforms in the top two panels of Fig. 5 around 100Hz . The curves in Fig. 5 correspond to the evolutions of only the point-particle contributions and for point-particle plus tidal contributions, both in ST theories. We see that tidal effects are more pronounced for the NS-NS than for the BH-NS system. The two curves for the NS-NS systems for low frequencies overlap. When the frequency starts to rapidly increase as shown in the bottom panel of Fig. 5, the tidal effects become more noticeable as can be seen in the phase difference between the curves in the middle panel for a NS-NS system. In principle, one might expect the scalar tidal effects to be larger for a BH-NS system, since a large difference between scalar charges maximises the dipolar flux (4.24). However, when one of the scalar charges vanishes, so do some of the tidal contributions to the phase, as a consequence of $\zeta_1 = \bar{\zeta}_1 = \tilde{\zeta}_1 = 0$ in this case, where the coefficients were defined in (3.8), (4.17), and (4.8). Furthermore we see from Fig. 5 that the effect of the tidal contributions mostly enters in the phase accumulation, while their effect on the amplitude is very small. The more irregular shape of the oscillations for the BH-NS case is due to more power being carried in modes besides the $(2, 2)$ mode for more asymmetric masses.

D. Identifying interesting parameter regimes

To gain insight into the importance of different tidal GW signatures we now focus on the Fourier phase evolution (4.43). We first survey a large part of the parameter space of NS-NS and BH-NS systems to analyse what systems are particularly interesting with respect to tidal effects on GWs in ST theory. Henceforth in the analysis we mainly focus on the intermediate SLy EoS and $\beta_0 = -4.5$ and comment on the dependency of the results on the EoS and β throughout the discussion.

For these parameter space studies we restrict to NS masses between $1 - 2M_\odot$, that is, roughly around the lightest and heavier observed NSs [92], and BH masses between $5 - 15M_\odot$, with the lower limit representing roughly the lowest mass of 'unambiguous BH candidates' from GW observations discussed in [3].

³ merger frequencies for NS-NS systems are usually around order 10^3Hz .

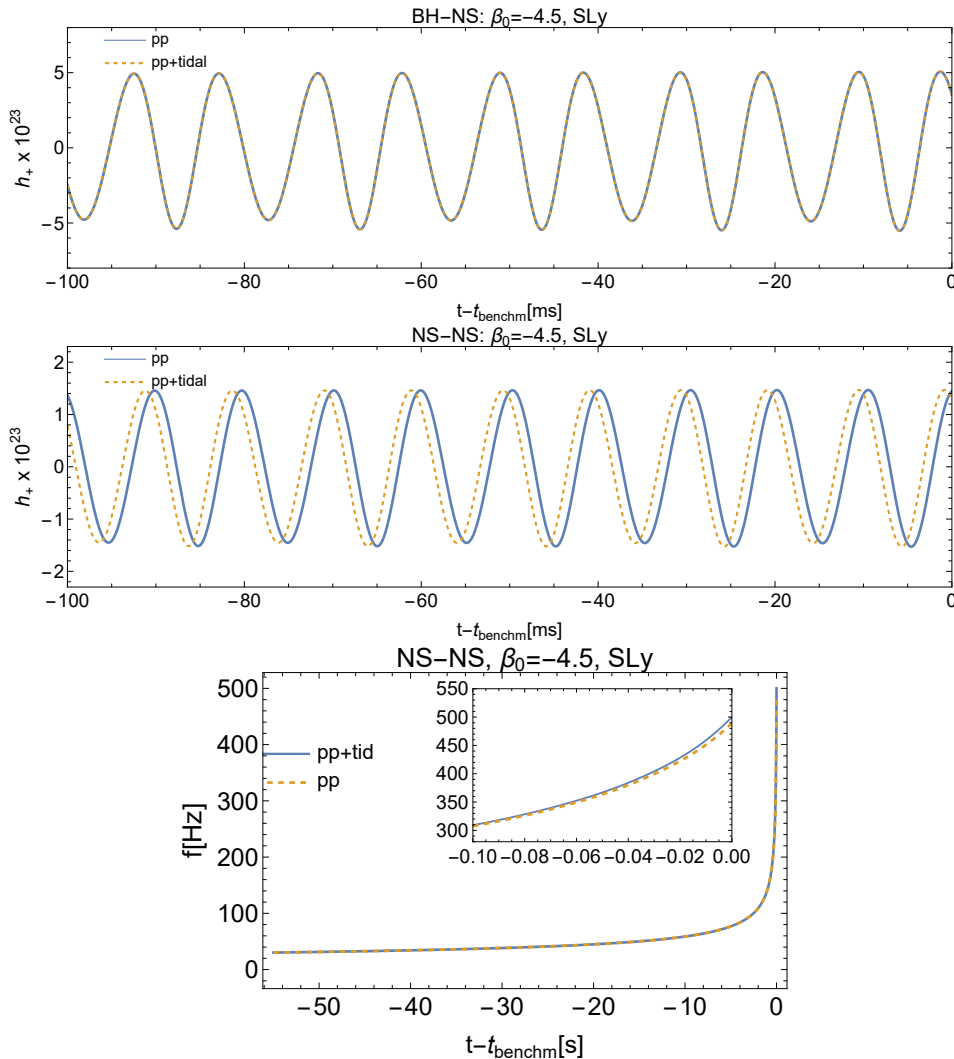


FIG. 5. The plus polarization of the time-domain waveform for a BH-NS system (top), NS-NS system (middle) and frequency evolution for the respective NS-NS system (bottom), assuming $\beta_0 = -4.5$ and the SLy EoS. The benchmark time $t_{\text{benchmark}}$ corresponds to the a frequency of $f_{\text{benchmark}} = 100\text{Hz}$ for the top two panels and $f_{\text{benchmark}} = 500\text{Hz}$ for the bottom panel. The inset in the bottom panel shows a zoom in of the curves near the benchmark time.

1. Estimated transition between DD and QD domains

We next consider the transition frequency between the regimes dominated by the dipole- and quadrupole losses discussed in Sec. IV E. Figure 6 shows the estimated transition frequency (4.33) for a wide parameter space of NS-NS systems. The dependence of (4.33) on S_- indicates that the transition frequency is highest when the difference between the two scalar charges is largest, as is also confirmed by the numerical sweep of the parameter space shown in Figure 6. The largest charge difference occurs in NS-NS systems when one NS has the maximum charge for which the corresponding mass M_q is identified from Fig. 3 and the companion NS is near the minimum mass within the range considered. Notably, we find that even for NS-NS systems with the largest S_- , the frequency

where the dipole dominates is $f_{\text{boundary}}^{DD} \lesssim 3\text{Hz}$, while for BH-NS binaries it is even lower due to their larger total mass. This implies that the *DD* regime lies below the lower end of the sensitive frequency band $f_{\text{low}} \sim 10\text{Hz}$ of current detectors [93] and even that of next-generation ground based GW detectors [94, 95]. Although (4.33) provides only a rough estimate of an extended range of frequencies where the transition occurs [49], these considerations motivate us to focus on the *QD* domain in the main part of this paper and delegate results for the *DD* regime to Appendix F. We also note that the *DD* regime has potential direct relevance for future deci-Hertz GW detectors, e.g. [96].

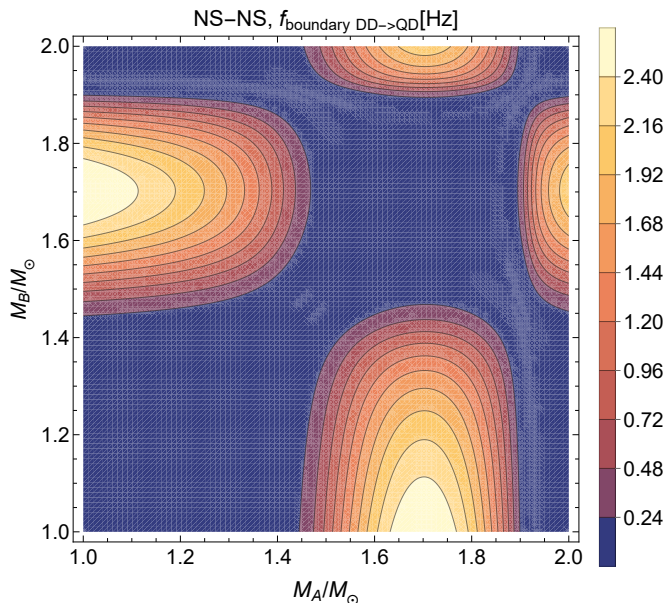


FIG. 6. Estimated transition frequency (4.33) for a NS-NS system between dipole- and quadrupole-driven regimes of the inspiral in the $M_A - M_B$ parameter space for $\beta_0 = -4.5$ and the SLy EoS. The color scale indicates the value of the estimated transition frequency in Hz.

2. Tidal Contributions to the QD Fourier phase

Next, we analyze the tidal contributions to the phase by computing the parameter dependencies of the various coefficients in (4.44). The results are summarized in Table I. We find that most of the coefficients, specifically S_-c_2 , c_3 , and $S_-^2c_4$, are strongly correlated with the scalar charge, while by contrast, the $\ell = 2$ non-dipolar coefficient involving the combination of $\tilde{\Lambda}$ and c_5 depends most strongly on the total mass. Depending on the system, the latter contribution also has the largest values of all tidal coefficients in the GW phase considered here.

Figure 7 shows examples of the dipolar contributions to tidal coefficients in (4.44). The upper panel is the dipolar piece of the $\ell = 2$ tidal terms for BH-NS systems characterized by $c_4S_-^2$, while the bottom panel shows the dipolar piece of the $\ell = 1$ coefficient, i.e. c_2S_- , for NS-NS systems. We re-iterate that as discussed above, in BH-NS systems, all $\ell = 1$ tidal effects vanish because they are purely scalar interactions and as the BH has no scalar charge, there is no scalar tidal field felt by the NS. However, we note that even for BH-NS, there is a nonvanishing dipolar contribution to the $\ell = 2$ tidal effects in the phase that arises from the energy fluxes.

For both types of binary systems, a comparison to Fig. 3 shows that the dipolar coefficients c_2S_- and $c_4S_-^2$ are largest when (one of) the NS(s) has a mass M_q corresponding to the configuration with the maximum scalar charge and the companion has the lowest mass M_{min} within the range considered. As the dipolar contributions

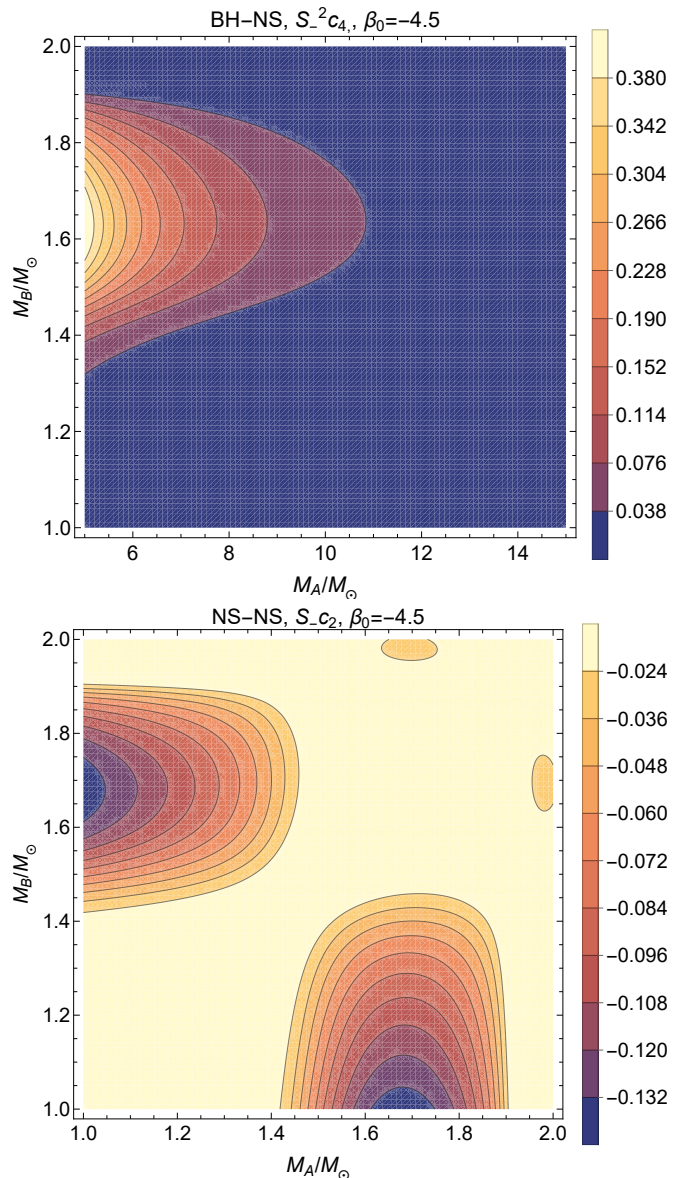


FIG. 7. Contour plots of two of the coefficients S_-c_2 and c_3 defined in (4.44), in the $M_A - M_B$ parameter space for $\beta_0 = -4.5$ and the SLy EoS for a BH-NS system (top) and NS-NS system (bottom). The plots for the coefficients of other powers of x in the phase can be found in Appendix E.

to (4.42) are directly proportional to S_- , the strong dependence on the scalar charge makes sense, maximizing S_- when the difference between scalar charges is largest. We also see from Fig. 7 that the sign of the dipolar tidal coefficient is negative for $\ell = 1$ (i.e. S_-c_2) but positive for $\ell = 2$ (i.e. $S_-^2c_4$). The analysis of all contributions to (4.44) in Appendix E further shows that for NS-NS systems, the magnitude of the $\ell = 2$ dipolar coefficient is about three orders of magnitude larger than for the $\ell = 1$ case.

In addition, in Appendix E we find that similarly

contribution to phase coefficients	largest for	zero for	sign	magnitude for NS-NS (\log_{10})
$c_2 S_-$ (scalar $\ell = 1$)	$(M_q, 1)$	$A = B,$ BH-NS	-	[-1, -2]
c_3 (scalar $\ell = 1$)	$(M_q, 1),$ (M_q, M_q)	BH-NS	+	[1, 2]
$c_4 S_-^2$ (all $\ell = 2$)	(M_q, M_{\min})	$A = B$	+	[1, 2]
$c_5 + 39\tilde{\Lambda}/(2\alpha^5 \xi^2)$ (all $\ell = 2$)	low M_{tot}	N/A	+	[4, 5]

TABLE I. Properties of the various tidal coefficients that appear with different powers of the frequency in the Fourier GW phasing (4.44) for binaries involving at least one NS. The notation $A = B$ refers to the case of two identical NSs. A dependence on S_- signals a contribution that arises through dipolar effects in the GW phase. The parentheses in the first column indicate the kinds of tidal interactions that contribute.

to the dipolar contributions discussed above, the non-dipolar coefficient c_3 is dominated by the dependence on the scalar charge and maximized for (M_q, M_{\min}) systems, however, it also has large values for systems around (M_q, M_q) . This is because although c_3 has no explicit dependence on S_- , it still involves $\zeta_1 \propto q_A^2 \lambda_{S,B}^{\ell=1} + (A \leftrightarrow B)$, which becomes large for maximized scalar charge systems around (M_q, M_q) . Overall, the values of c_3 for the considered parameter space are positive and of order $10^1 - 10^2$.

By contrast, the non-dipolar quadrupolar coefficient characterizing the relative $O(x^5)$ contributions to the phase (4.44) shows little correlations with the scalar charge but instead depends most strongly on the mass, with the maximum value occurring for the lowest total mass. This tidal coefficient is negative and of order $10^4 - 10^5$ for the parameter space considered here. For BH-NS systems, the qualitative behavior is similar but the overall magnitude is lower $\sim 10^2 - 10^3$ because of the larger total mass of these systems. These results indicate that the tensor tidal contributions (that enter as terms of the form $M_B \lambda_{T,A}^{\ell=2} + (A \leftrightarrow B)$ in the parameter $\tilde{\zeta}_2$ and the phase (4.42)) to the phase dominate, as also expected from the tidal deformability curves of Fig. 3. This too is reflected in the overall dominant magnitude of the $O(x^5)$ coefficient compared to the other tidal terms in (4.44), which is also the only nonvanishing contribution in the limit of GR.

Based on the above analysis of the parameter space of tidal coefficients, we choose three representative cases for each type of binary system for further analysis: one each that maximizes the $\ell = 1, 2$ tidal effects respectively, and another where all tidal coefficients take intermediate values (though note that as explained above, some of them are always zero for NS-BH). These choices are listed in Table II.

Scenario $S1$ maximizes the contribution of the quadrupolar contributions involving $\tilde{\Lambda}$ and c_5 and is free

scenario	tidal terms	binary	$M_A(M_\odot)$	$M_B(M_\odot)$
S1	no dipole & max $\ell = 2$	NS-NS	1	1
		BH-NS	5	1
S2	max dipole	NS-NS	1	M_q
		BH-NS	5	M_q
S3	intermediate	NS-NS	1.1	1.2
		BH-NS	8.9	1.2

TABLE II. Properties of binary systems considered for the case studies. We consider three scenarios to cover two extremes and an intermediate case within the parameter space described in the text and with $M_q \sim 1.7M_\odot$ here.

from dipolar contributions, since they vanish for an equal NS case as $S_- = 0$. Scenario $S2$ maximizes the effects of the dipolar contributions proportional to S_- together with the non-dipolar scalar tidal effects encapsulated in c_3 , and Scenario $S3$ is an intermediate case, close but not equal to the identical-NS limit, in order to avoid cancellations of terms scaling as $(q_A - q_B)$.

E. Tidal effects on the GW phase evolution

To analyze the effects of different tidal contributions on the GWs, we focus on the Fourier domain phase evolution in the QD domain.

1. Difference in net tidal effects between ST and GR

The left panel of Figure 8 shows the difference between the GR Fourier phase and the ST phase in the quadrupolar driven domain (4.42) including corrections up to relative 1PN order. The evolutions of the point particle phase in ST and GR, denoted by the blue curves, are matched using the freedom in initial conditions for (4.42) to find the initial orbital phase and time that minimize the integral of the absolute value of the difference squared over the frequency domain 9 – 10Hz. For the tidal contributions (red curves) we only used the freedom in initial phase angle to set the phase contributions equal to zero at the starting frequency of 10Hz. We chose this approach for the tidal contributions as the dependency on the frequency for the ST tidal contributions is qualitatively different from the GR tidal terms, hence their evolutions as function of the frequency are hard to align over a frequency range. Do note that in the case of the tidal phase difference shown in the left panel of Fig. 8 there is an additional free initial condition t_0 which we now set to zero. We find that, as expected, the difference in point particle contributions is many orders of magnitude larger than the tidal contributions, with the largest point-particle differences for Scenario S2, where the dipolar scalar radiation is maximized.

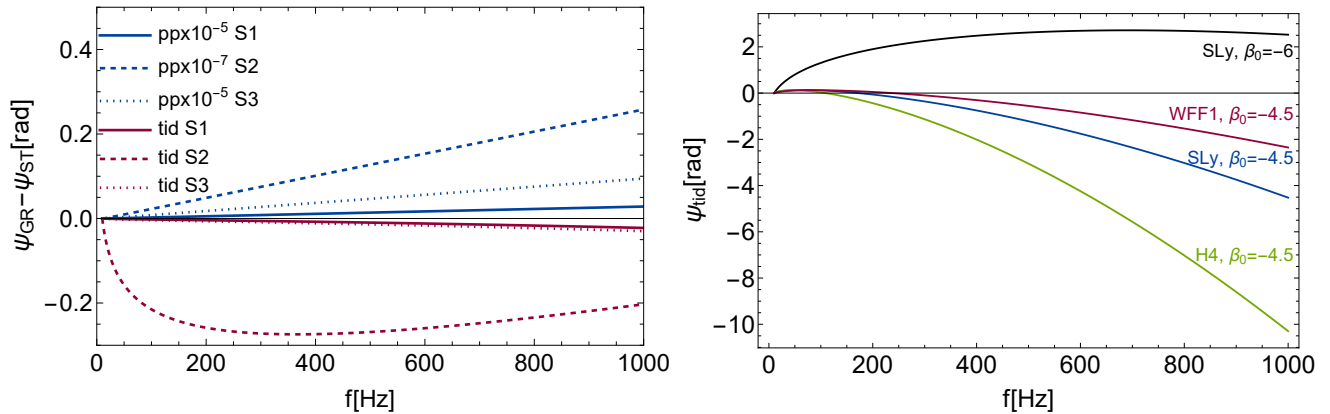


FIG. 8. *Left panel*: Difference between GR and ST Fourier phase as a function of frequency for NS-NS binaries. The blue lines correspond to the point particle (pp) contributions and the red ones to the tidal contributions. The solid, dashed and dotted lines indicate the different scenarios S1, S2 and S3 respectively. Note that the point-particle curves are rescaled by many orders of magnitude to show them on the same plot. The pp phase evolutions were aligned in the window of 9 – 10Hz. *Right panel*: the tidal contribution of the ST Fourier phase for NS-NS binary of S2 for different EoS and β_0 . The tidal phase functions in both panels were set to zero at 10Hz with the freedom in initial phase angle (4.42).

For the tidal contributions, the phase difference between GR and ST is negative, indicating that the net tidal effects in ST theory are smaller than in GR. This is because in GR, only the quadrupolar tensor tidal effects appear and lead to a negative contribution to the phase, indicating that the inspiral is faster and hence accumulates less phase per frequency interval than the point-particle scenario. By contrast, in ST theories, tidal effects in the GW phase include dipolar and quadrupolar scalar, tensor and scalar-tensor contributions having different signs. These combine to yield a total tidal phase correction that is smaller in magnitude than that in GR.

In particular, the main sources of the differences between tidal effects in GR and ST theories are the scalar and scalar-tensor tidal contributions. Scenario S2 maximizes these contributions and we see from the dashed red curve in Fig 8 that it indeed leads to the largest differences. The different shape of the S2 curve in the left panel can be explained together with the blue curve in the right panel. The right panel of Fig. 8 shows the ST tidal fourier phase contributions for different EoS and choices of β_0 in S2. The blue curve corresponds to the choices of parameters adopted in the left panel. We find that in this scenario, not only do the additional scalar and scalar tensor tidal contributions make the total tidal contributions smaller than in GR, also the sign becomes positive in the frequency window from 0 – 200Hz. This positive evolution sharply increases the difference with the negative GR tidal phase evolution shown with the dashed curve in the left panel. Beyond 200Hz the ST tidal phase contribution also becomes negative again and starts to decrease its difference with GR. In the other scenarios the ST tidal contributions with a positive sign are less prominent and the total ST tidal phase stays negative over the whole frequency domain, showing a small

offset with the GR tidal phase contribution in the left panel. In Scenario S1 (solid red curve) the quadrupolar tensor tidal contributions are maximized, however this contribution differs only slightly from the GR contribution via the small change in the quadrupolar tensor tidal deformability. In this Scenario the other tidal contributions are minimal and therefore also the difference with GR is smallest for this system.

In the right panel of Fig. 8 we show the effect of a stiffer (H4) respectively softer EoS (WFF1) and a larger value for $-\beta_0$ on the ST tidal contributions to the Fourier phase in S2. We find that for a stiffer EoS, the magnitude of the tidal contributions increases, which corresponds to the tidal deformabilities being larger for a stiffer EoS [45]. For a larger value of $-\beta_0$ the positive sign tidal contributions to the total phase are severely amplified leading to a positive tidal phase contribution over the whole frequency range. It is interesting to note that while one might in general expect ST effects for larger $|\beta_0|$ to be larger, we see here that the net tidal effects are of the same order of magnitude, except for the sign difference. This is because the comparison here is done at fixed NS masses, which correspond to the configurations that maximize the dipole effects for $|\beta_0| = 4.5$ while the maximum dipole configuration for $|\beta_0| = 6$ occurs for different masses.

2. Effect of scalar, tensor, and mixed tidal deformabilities

It is further interesting to consider the effect of the different scalar, tensor, and mixed scalar-tensor tidal interactions on the net tidal phase. Fig. 9 shows the different contributions of the corresponding tidal deformabilities that make up the c parameters of (4.44) for dif-

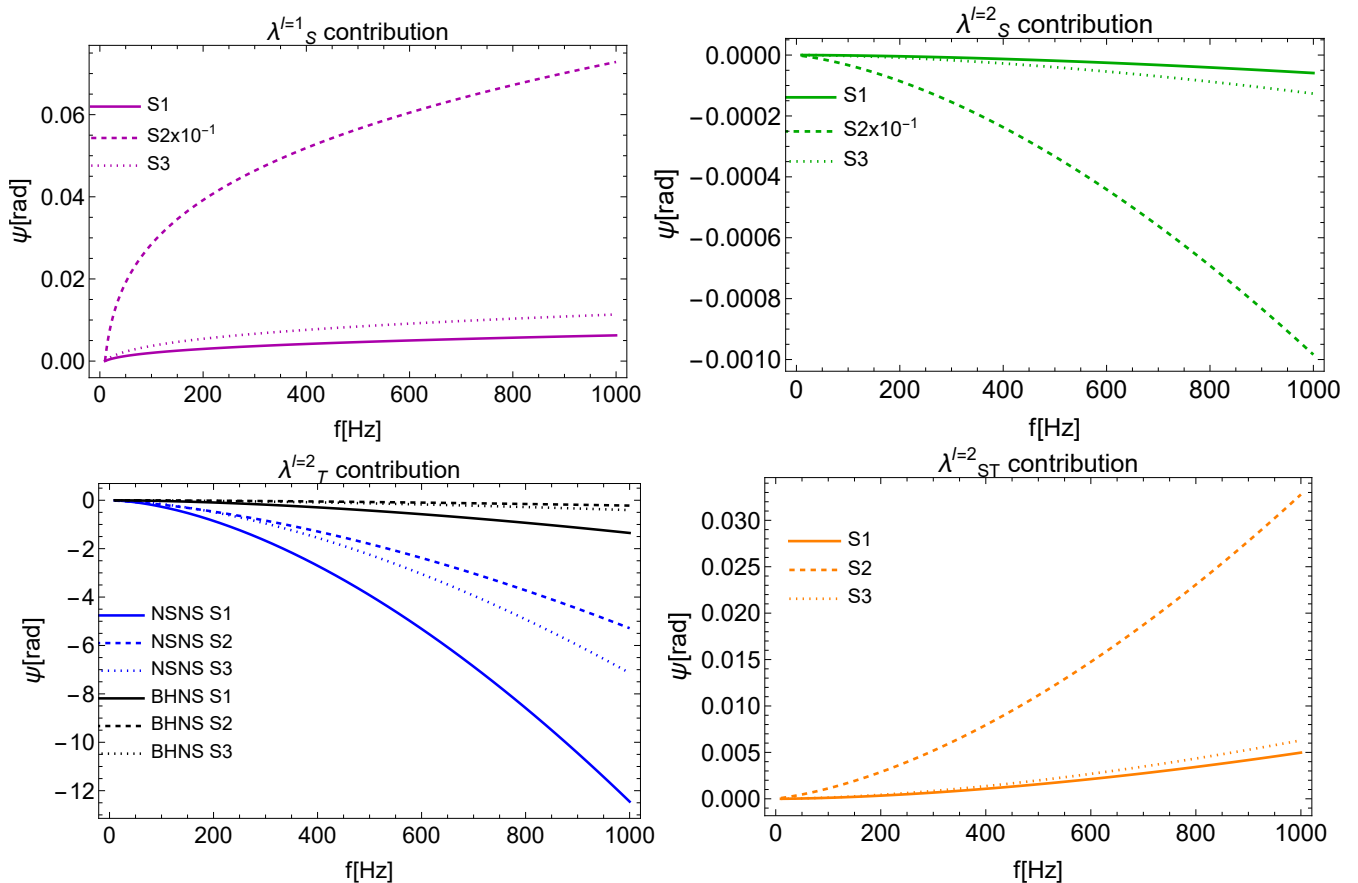


FIG. 9. Different contributions of the tidal deformabilities to the Fourier phase (4.43). In each panel the solid, dashed and dotted curve correspond to the systems of Scenario S1, S2 and S3 respectively for the NS-NS systems. The bottom left plot also shows these scenarios for BH-NS systems in black.

ferent scenarios of NS-NS and BH-NS systems for the quadrupolar driven phase tidal effects. To generate these plots, we isolate the terms proportional to the different tidal deformabilities in (4.42) and (4.43). We terminate the phase evolution at a chosen benchmark frequency of 1kHz for illustration, although the approximations made to derive our results become invalid before then.

Comparing the panels of Fig. 9 we find that in all studied cases the dipolar ($\ell = 1$) scalar tidal contributions and the quadrupolar ($\ell = 2$) scalar-tensor contributions come with a positive sign and the quadrupolar scalar and quadrupolar tensor with negative sign, meaning that they slow down and speed up the inspiral respectively.

Furthermore, we find for all NS-NS scenarios that the quadrupolar tensor tidal contributions dominate over the others, as was already predicted from the analysis in Sec. VD 2. Also, comparing the quadrupolar tensor contributions for the NS-NS and BH-NS cases, we find that the phase contribution in the BH-NS case is around an order of magnitude smaller because of the larger total mass of these systems. Generally, the qualitative behaviour of the tidal contributions is the same for the other EoSs, only the magnitude of the accumulated Fourier phase is

slightly shifted, with slightly larger effects for H4 and slightly smaller effects for WFF1 related to the shift in order of magnitude of the tidal deformability which is bigger for the stiffer EoS H4 and smaller for the softer EoS WFF1. For $\beta_0 = -6$ the same conclusion holds however the effects are more prominent as the accumulated phase increases around one order of magnitude. We also see from Fig. 9 that the choices of scenarios summarized in Table II have the expected effects, with the largest the tensor quadrupole effects for S1 and the largest dipolar scalar and quadrupolar scalar and scalar-tensor contributions for S2, while S3 described an intermediate case. Hence, we conclude that for studying the tidal effects specifically present in scalar tensor theory (scalar dipolar and quadrupolar scalar and scalar-tensor tidal effects) a system that maximizes the difference between the two scalar charges of the two bodies is preferred. This also corresponds to what we found for the added contribution in Fig. 8.

3. Discussion

The fact that the tidal phase difference with GR in Fig. 8 is negative means that there could be degeneracies between the ST accumulated tidal effects to the phase and the GR tidal contributions for the same system but with a softer EoS also giving smaller tidal contributions. However, the large difference for the point particle contributions would still resolve two situations. Additionally, as the difference in tidal contributions stays below a magnitude of 1 rad they are unlikely to be resolvable with the current GWs detectors. Still the degeneracy with GR might be a problem for other beyond-GR theories with scalarized NSs for which omitting the scalar and scalar-tensor tidal effects could potentially lead to biases in the inferred properties of the compact objects from GW observations, especially for systems with large differences between the scalar charges of the bodies. Furthermore, from comparing the top left and bottom right panels of Fig. 9 the magnitude of the dipolar scalar tidal contributions for S1 and S3 are of the same order as the quadrupolar scalar-tensor contributions, hence when including the scalar tidal contributions the interaction with the tensor field cannot be neglected.

VI. SUMMARY AND CONCLUSION

In this paper, we studied tidal signatures in GWs from NS binary systems in scalar-tensor theories of gravity where sufficiently compact NSs can give rise to a scalar condensate. Building on [45], which showed that in ST theories, tidal effects are characterized by three different kinds of tidal deformability coefficients for the scalar, tensor, and mixed sector arising from the nonlinear coupling between gravity, scalar field, and baryonic matter, we used analytical approximations in finite-size and PN corrections in the early inspiral to compute tidal effects in the GWs.

We showed that in addition to a tidal term similar to GR, there are also terms that scale with lower powers of the frequency and involve different combinations of tidal coefficients. Specifically, we showed that the Fourier GW phase in the regime of greatest interest for current and next-generation ground-based GW detectors can be written as

$$\psi_{\text{tid}} = \frac{3}{128\eta x^{5/2}} [c_2 S_- x^2 + c_3 x^3 + c_4 S_-^2 \left(\log x - \frac{2}{3} \right) x^4 + \left(\frac{39}{2\alpha^5 \xi^2} \tilde{\Lambda} + c_5 \right) x^5], \quad (6.1)$$

where the various coefficients c_i for $i = 2, 3, 4, 5$ are given explicitly in terms of masses, scalar charges, and tidal deformabilities of the bodies in (C1)–(C4), and α and ξ were defined in (3.7) and (4.39), with S_{\pm} given in (4.23) and $\tilde{\Lambda}$ having the same functional form (4.45) in terms of mass-weighted combinations of quadrupolar tensor tidal

deformabilities as in GR. We also recall that in ST theories, the frequency-parameter x defined in (3.13) differs from its GR counterpart by a factor of $\alpha^{2/3}$ corresponding to a renormalization of the gravitational interaction.

We then specialized to a Gaussian coupling function for the ST theory and surveyed binary systems over a range of parameter space to identify interesting scenarios that maximize the different tidal contributions. In general we found that due to different signs associated with the different types of tidal effects in the GW phase (c.f. Table I), the net tidal signatures in ST gravity are smaller than in GR. This could in principle lead to degeneracies with changes in the EoS of the NSs to a softer one but conclusions about this issue will require further work. We also showed that the difference with GR tidal effects is largest for systems with the largest asymmetry in scalar charges and analyzed the effects of changing the EoS and the theory-parameter β_0 for a binary system of fixed masses.

By systematically studying each tidal contribution to the Fourier phase, we further demonstrated that, at quadrupolar order, the scalar-tensor tidal deformability has a larger effect on GWs than the scalar tidal deformability and therefore should be accounted for when also considering the scalar tidal deformability. Furthermore, depending on the parameters, the different contributions that come with different powers of frequency can lead to a non-monotonic behavior of the tidal phase evolution as a function of frequency. Quantitatively, the difference in tidal effects on the phase between ST and GR stays of order 10^{-1} rad and is therefore difficult to resolve with current detectors. It is also many orders of magnitude smaller than the differences in point-particle inspirals, which would directly indicate modifications to GR and hence reduce potential degeneracies with EoS effects in the small tidal corrections.

While our case studies led to quantitative insights into the impact of the dominant adiabatic tidal phenomena in particular ST theories, our main aim was to develop the methodology for understanding and modeling tidal GW signatures from scalarized compact objects in theories of gravity beyond GR, which lead to richer features. Our methods have broad applications to a wider range of proposed classes of theories, though the details of the GW phase contributions will be theory-dependent. This work opens several avenues for further studies. For instance, our results could be used for data analysis to put constraints on the parameter space covered by ST theories. It would also be interesting to compare our results, combined with higher PN order point-particle terms from [68] to the numerical calculations of BH-NS binaries in ST theories [51] or others for NS-NS systems, to include a mass of the scalar field as the lowest order self-interaction, to consider dynamical tides, and tidal signatures in GWs in other classes of beyond-GR theories.

VII. ACKNOWLEDGEMENTS

We thank Justin Janquart for insightful discussions. G.C., and T.H. acknowledge funding from the Nederlandse Organisatie voor Wetenschappelijk Onderzoek (NWO) sectorplan. I.G. acknowledges the Dutch Black Hole Consortium (project NWA 1292.19.202) part of the National Research Agenda

Appendix A: Useful identities involving symmetric trace-free tensors

Here, we summarize several identities used in the derivations discussed in the main text. In this appendix we set $r = |\mathbf{x}|$ with \mathbf{x} a separation vector. The result of taking ℓ derivatives of $1/r$ can be written as

$$\partial_L \frac{1}{r} = (-1)^\ell (2\ell - 1)!! \frac{n_{\langle L} \rangle}{r^{\ell+1}}, \quad (\text{A1})$$

where $\mathbf{n} = \mathbf{x}/r$ is a unit vector. This was used to obtain explicit expressions for the tidal fields in (3.4). In the tidal Lagrangian (2.17) we needed the contraction of two tidal tensors and hence STF unit vectors, which simplifies via the identity

$$n_{\langle L} \rangle n^{\langle L \rangle} = \frac{\ell!}{(2\ell - 1)!!}. \quad (\text{A2})$$

To derive the tidal contributions to the acceleration required the additional identities

$$\partial_i \left(\partial_L \frac{1}{r} \right)^2 = -2 \frac{(2\ell - 1)!! (\ell + 1)!}{r^{2\ell+3}} n^i, \quad (\text{A3})$$

and

$$n_{\langle L} \rangle n^{\langle iL \rangle} = \frac{(\ell + 1)!}{(2\ell + 1)!!} n^i. \quad (\text{A4})$$

Appendix B: Full expressions for the binary dynamics, waveforms and GW phase

In this appendix, we provide the complete expressions for various quantities to 1PN order in the point-mass sector and leading order in tidal effects.

a. Binary dynamics

In Sec. III A we discussed how to obtain the leading-order tidal corrections to the binary dynamics. Together with the point particle 1PN contributions, the two-body Lagrangian is given by

$$\begin{aligned} L_{AB} = & -M_A + \frac{1}{2} M_A \mathbf{v}_A^2 + \frac{G\alpha M_A M_B}{2r} + \left(\frac{1}{8} M_A \mathbf{v}_A^4 \right. \\ & + \frac{G\alpha M_A M_B}{r} \left[-\frac{G\alpha M_A}{2r} (1 + 2\bar{\beta}_B) + \frac{3}{2} (\mathbf{v}_A^2) \right. \\ & \left. \left. - \frac{7}{4} (\mathbf{v}_A \cdot \mathbf{v}_B) - \frac{1}{4} (\mathbf{n} \cdot \mathbf{v}_A) (\mathbf{n} \cdot \mathbf{v}_B) + \frac{\bar{\gamma}}{2} (\mathbf{v}_A - \mathbf{v}_B)^2 \right] \right) \\ & + \frac{1}{2} G^2 \mu M \alpha^2 \sum_{\ell} \frac{(2\ell - 1)!!}{2r^{2(\ell+1)}} \zeta_{\ell} + (A \leftrightarrow B), \end{aligned} \quad (\text{B1})$$

where we use boldface to indicate spatial vectors and define

$$\bar{\gamma} \equiv -2 \frac{q_A q_B}{\alpha}, \quad \bar{\beta}_{A/B} \equiv \frac{1}{2} \frac{\beta_{A/B} q_{B/A}^2}{\alpha^2}, \quad (\text{B2})$$

$$\beta_{\pm} \equiv \frac{\bar{\beta}_A \pm \bar{\beta}_B}{2}. \quad (\text{B3})$$

The relative acceleration obtained from (B1) is

$$\begin{aligned} \mathbf{a} = & -\frac{G\alpha M}{r^2} \mathbf{n} + \frac{G\alpha M}{r^2} \left\{ \mathbf{n} \left[\frac{3}{2} \eta \dot{r}^2 - (1 + 3\eta + \bar{\gamma}) \mathbf{v}^2 \right] \right. \\ & + 2\mathbf{v}\dot{r} [2 - \eta + \bar{\gamma}] + \frac{2G\alpha M \mathbf{n}}{r} \left[2 + \eta + \bar{\gamma} + \beta_+ - \frac{\Delta M}{M} \beta_- \right] \\ & \left. - G^2 \alpha^2 M \sum_{\ell} \frac{(2\ell - 1)!! (\ell + 1)}{r^{2\ell+3}} \mathbf{n} \zeta_{\ell} \right\}. \end{aligned} \quad (\text{B4})$$

The radial component of the equations of motion (B4) for circular orbits with $\dot{r} = \ddot{r} = 0$ lead to the angular frequency

$$\begin{aligned} \omega^2 = & \frac{G\alpha M}{r^3} \left[1 - \frac{\alpha M}{r} \left(3 - \eta - \frac{2\beta_- \Delta M}{M} + 2\beta_+ \right. \right. \\ & \left. \left. + \bar{\gamma} - \sum_{\ell} \frac{(\ell + 1)(2\ell - 1)!!}{r^{2\ell} M} \zeta_{\ell} \right) \right], \end{aligned} \quad (\text{B5})$$

with $\Delta M \equiv M_A - M_B$. Inverting this expression perturbatively and expressing ω in terms of the PN parameter x defined in (3.13) yields

$$\begin{aligned} r(x) = & \frac{G\alpha M}{x} \left[1 - \frac{1}{3} x \left(3 - \eta + \bar{\gamma} + 2\beta_+ - 2 \frac{\Delta M}{M} \beta_- \right. \right. \\ & \left. \left. + \sum_{\ell} \frac{(2\ell - 1)!! (\ell + 1)}{G^{2\ell} \alpha^{2\ell} M^{1+2\ell}} x^{2\ell} \zeta_{\ell} \right) \right]. \end{aligned} \quad (\text{B6})$$

Using this result and the energetics from the Lagrangian (B1) we obtain for the binding energy to the orders of approximation we are considering

$$\begin{aligned} E(x) = & -\frac{\mu x}{2} \left[1 + \frac{2}{3} x \left(\beta_+ - \frac{\Delta M}{M} \beta_- - \bar{\gamma} - \frac{9 + \eta}{8} \right) \right. \\ & \left. - \frac{1}{3} \sum_{\ell} (2\ell - 1)!! (4\ell + 1) \frac{G^{-2\ell} \zeta_{\ell}}{M^{2\ell+1} \alpha^{2\ell}} x^{2\ell+1} \right]. \end{aligned}$$

b. Scalar and tensor waves

In Sec. IV we discuss how one obtains the Newtonian tidal corrections to the scalar and tensor waveform. Together with the 1PN point particle terms the scalar waveform is given by

$$\delta\varphi = \frac{G\mu\sqrt{\alpha}}{d} \left\{ P^{-1/2} \tilde{\Phi} + \tilde{\Phi} + P^{1/2} \tilde{\Phi} + P^{1/2} \tilde{\Phi}_{tid} \right\}, \quad (\text{B7})$$

here the superscript of P denotes the PN order of the coefficients. The coefficients are given by

$$\begin{aligned}
P^{-1/2}\tilde{\Phi} &= 2\mathcal{S}_-(\mathbf{n}\cdot\mathbf{v}) \\
\tilde{\Phi} &= \left(\mathcal{S}_+ - \frac{\Delta M}{M}\mathcal{S}_-\right) \left[-\frac{G\alpha M}{r} \left(\frac{\mathbf{n}\cdot\mathbf{r}}{r}\right)^2 + (\mathbf{n}\cdot\mathbf{v})^2 - \frac{1}{2}v^2\right] + \frac{G\alpha M}{r} \left[-2\mathcal{S}_+ + \frac{8}{\bar{\gamma}}(\mathcal{S}_+\beta_+ + \mathcal{S}_-\beta_-)\right], \\
P^{1/2}\tilde{\Phi} &= \left(-\frac{\Delta M}{M}\mathcal{S}_+ + (1-2\eta)\mathcal{S}_-\right) \left[\frac{3}{2}\frac{G\alpha M}{r^4}\dot{r}(\mathbf{n}\cdot\mathbf{r})^3 - \frac{7}{2}\frac{G\alpha M}{r^3}(\mathbf{n}\cdot\mathbf{v})(\mathbf{n}\cdot\mathbf{r})^2 + (\mathbf{n}\cdot\mathbf{v})^3\right] \\
&\quad + (\mathbf{n}\cdot\mathbf{v}) \left\{ \left(\frac{\Delta M}{M}\mathcal{S}_+ - \eta\mathcal{S}_-\right)v^2 + \frac{G\alpha M}{r} \left[\frac{1}{2}\frac{\Delta M}{M}\mathcal{S}_+ + \left(2\eta - \frac{3}{2}\right)\mathcal{S}_- \right. \right. \\
&\quad \left. \left. - \frac{4}{\bar{\gamma}}\frac{\Delta M}{M}(\mathcal{S}_+\beta_+ + \mathcal{S}_-\beta_-) + \frac{4}{\bar{\gamma}}(\mathcal{S}_-\beta_+ + \mathcal{S}_+\beta_-)\right] \right\} \\
&\quad + \frac{G\alpha M}{r^2}\dot{r}(\mathbf{n}\cdot\mathbf{r}) \left[\frac{3}{2}\mathcal{S}_- - \frac{5}{2}\frac{\Delta M}{M}\mathcal{S}_+ + \frac{4}{\bar{\gamma}}\frac{\Delta M}{M}(\mathcal{S}_+\beta_+ + \mathcal{S}_-\beta_-) - \frac{4}{\bar{\gamma}}(\mathcal{S}_-\beta_+ + \mathcal{S}_+\beta_-)\right] \\
P^{1/2}\tilde{\Phi}_{tid} &= \sum_{\ell} \sum_{k=0}^{\ell} \sum_{p=1}^k \frac{GN^L\bar{\zeta}_{\ell}}{\sqrt{\alpha\mu}} \frac{(2\ell+p)!(-1)^{p+\ell}}{k!(\ell-k)!2^{\ell}} \times \frac{\partial_t^{\ell-k} r_{<L>}}{r^{2\ell+p+1}} B_{k,p}(\dot{r}, \ddot{r}, \dots, r^{k-p+1}).
\end{aligned} \tag{B8}$$

The tensor waveform has the form

$$h_{TT}^{ij} = \frac{2G\mu}{d} \{Q^{ij}\}_{TT} = \frac{2G\mu}{d} \left\{ \tilde{Q}^{ij} + P^{1/2}\tilde{Q}^{ij} + \left(P\tilde{Q}^{ij} + P\tilde{Q}_{tid}^{ij}\right) \right\}_{TT} \tag{B9}$$

with $\{\dots\}_{TT}$ denoting the TT projection and

$$\begin{aligned}
\tilde{Q}^{ij} &= 2 \left[v^{ij} - \frac{GM\alpha r^{ij}}{r^3} \right], \\
P^{1/2}\tilde{Q}^{ij} &= \frac{\Delta M}{M} \left[3\frac{GM\alpha}{r^3}(\hat{\mathbf{n}}\cdot\mathbf{r}) \left(2v^{(i}r^{j)} - \frac{\dot{r}r^{ij}}{r} \right) - (\hat{\mathbf{n}}\cdot\mathbf{v}) \left(2v^{ij} - \frac{GM\alpha r^{ij}}{r^3} \right) \right], \\
P\tilde{Q}^{ij} &= \frac{1-3\eta}{3} \left\{ (\mathbf{r}\cdot\hat{\mathbf{n}})^2 \frac{G\alpha M}{r^3} \left[\left(6\bar{E} - 15\dot{r}^2 + 13\frac{G\alpha M}{r} \right) \frac{r^{ij}}{r^2} + 30\dot{r} \frac{r^{(i}v^{j)}}{r} - 14v^{ij} \right] \right. \\
&\quad \left. + (\hat{\mathbf{n}}\cdot\mathbf{v})^2 \left[6v^{ij} - 2\frac{G\alpha M}{r^3}r^{ij} \right] + \frac{1}{2}(\mathbf{r}\cdot\hat{\mathbf{n}})(\hat{\mathbf{n}}\cdot\mathbf{v}) \frac{G\alpha M}{r^2} \left[12\frac{\dot{r}r^{ij}}{r^2} - 32\frac{r^{(i}v^{j)}}{r} \right] \right\} \\
&\quad + \frac{1}{3} \left\{ \left[3(1-3\eta)v^2 - 2(2-3\eta)\frac{G\alpha M}{r} \right] v^{ij} + 4\frac{G\alpha M}{r} (5+3\eta+3\bar{\gamma}) \frac{\dot{r}}{r} r^{(i}v^{j)} \right. \\
&\quad \left. + \frac{G\alpha M}{r^3} r^{ij} \left[3(1-3\eta)\dot{r}^2 - (10+3\eta+6\bar{\gamma})v^2 + \left(29+12\bar{\gamma}+12\beta_+ - 12\frac{\Delta M}{M}\beta_- \right) \frac{G\alpha M}{r} \right] \right\}, \\
P\tilde{Q}_{tid}^{ij} &= - \sum_{\ell} \frac{2G^2\alpha^2 M^2(1+\ell)(2\ell-1)!!\bar{\zeta}_{\ell}}{r^{2(2+\ell)}} r^i r^j \\
&\quad + \sum_{\ell=2}^{\ell} \sum_{k=0}^{\ell} \sum_{p=1}^k \frac{2GN^{L-2}\bar{\zeta}_{\ell}}{\mu} \frac{(2\ell+p)!(-1)^{p+\ell}}{k!(\ell-k)!2^{\ell}} \frac{\partial_t^{\ell-k} r_{<L>}}{r^{2\ell+p+1}} B_{k,p}(\dot{r}, \ddot{r}, \dots, r^{k-p+1}),
\end{aligned}$$

with $\bar{E} = v^2/2 - Gm\alpha/r$ the leading order binding energy in CM coordinates [65, 75]. In Sec. IV D we take the

angular integral of the square of the time derivative to the waveforms to obtain the scalar and tensor energy flux. The scalar flux up to 1PN is given by

$$\begin{aligned}
\mathcal{F}_S = & \frac{\eta^2}{G\alpha} \left(\frac{G\alpha M}{r} \right)^4 \left[\frac{4}{3} \mathcal{S}_-^2 + \frac{8}{15} \left(\frac{G\alpha M}{r} \left[\left(-23 + \eta - 10\bar{\gamma} - 10\beta_+ + 10 \frac{\Delta M}{M} \beta_- \right) \mathcal{S}_-^2 \right. \right. \right. \\
& - 2 \frac{\Delta M}{M} \mathcal{S}_+ \mathcal{S}_- \left. \left. \left. + v^2 \left[+2\mathcal{S}_+^2 + 2 \frac{\Delta M}{M} \mathcal{S}_+ \mathcal{S}_- + (6 - \eta + 5\bar{\gamma}) \mathcal{S}_-^2 - \frac{10}{\bar{\gamma}} \frac{\Delta M}{M} \mathcal{S}_- (\mathcal{S}_+ \beta_+ + \mathcal{S}_- \beta_-) \right. \right. \right. \right. \\
& + \frac{10}{\bar{\gamma}} \mathcal{S}_- (\mathcal{S}_- \beta_+ + \mathcal{S}_+ \beta_-) \left. \left. \left. \right] + \dot{r}^2 \left[+ \frac{23}{2} \mathcal{S}_+^2 - 8 \frac{\Delta M}{M} \mathcal{S}_+ \mathcal{S}_- + \left(9\eta - \frac{37}{2} - 10\bar{\gamma} \right) \mathcal{S}_-^2 - \frac{80}{\bar{\gamma}} \mathcal{S}_+ (\mathcal{S}_+ \beta_+ \right. \right. \right. \\
& + \mathcal{S}_- \beta_-) + \frac{30}{\bar{\gamma}} \frac{\Delta M}{M} \mathcal{S}_- (\mathcal{S}_+ \beta_+ + \mathcal{S}_- \beta_-) - \frac{10}{\bar{\gamma}} \mathcal{S}_- (\mathcal{S}_- \beta_+ + \mathcal{S}_+ \beta_-) + \frac{120}{\bar{\gamma}^2} (\mathcal{S}_+ \beta_+ + \mathcal{S}_- \beta_-)^2 \left. \left. \left. \right] \right] \right) \\
& + \frac{4S_-}{3M^2 \eta \alpha^{3/2} r^2} \left(9\dot{r} - 3v^2 + \frac{2GM\alpha}{r} \right) \bar{\zeta}_1 + \frac{8GS_-^2 \alpha}{3r^3} \left(2\zeta_1 + 9 \frac{\zeta_2}{r^2} \right) \left. \right]. \tag{B10}
\end{aligned}$$

Assuming circular orbits we can write the scalar flux in terms of PN parameter x defined in (3.13) as

$$\mathcal{F}_S(x) = x^4 [S4 + x (S5 + S5_{\text{tid},1} x^2 + S5_{\text{tid},2} x^4)], \tag{B11}$$

with

$$\begin{aligned}
S4 &= \frac{4\eta^2 S_-^2}{3\alpha G}, \\
S5 &= \left(\frac{8\eta^2 S_-}{45\alpha G} \right) \left(\frac{15}{4\alpha^{3/2} M} (\Delta M q_B \beta_A - M q_B \beta_A + \Delta M q_A \beta_B + M q_A \beta_B) + 10 \frac{\Delta M}{M} S_- \beta_- \right. \\
& \quad \left. - S_- (5\bar{\gamma} + 10\beta_+ + 10\eta + 21) + \frac{6S_+^2}{S_-} \right), \\
S5_{\text{tid},1} &= \left(-\frac{4S_- \mu \bar{\zeta}_1}{3\alpha^{9/2} G^3 M^5} + \frac{16S_-^2 \mu^2 \zeta_1}{9\alpha^3 G^3 M^5} \right), \\
S5_{\text{tid},2} &= \frac{S_-^2 \mu^2 \zeta_2}{\alpha^5 G^5 M^7}. \tag{B12}
\end{aligned}$$

Note that our notation here differs from [64, 65, 67] as we have the expressed several terms in S5 explicitly in terms of the scalar charge q , while [64, 65, 67] rewrite them as a term proportional to $1/\bar{\gamma}$. This has the drawback that for a BH-NS system, with the black hole having zero scalar charge, the parameter $\bar{\gamma}$ vanishes and causes an apparent divergence in the expressions from [64, 65, 67]. Here, we have explicitly expanded the dependencies on $1/\bar{\gamma}$ in terms of the constituent parameters such as the scalar charge and β , which leads to manifestly finite expressions in the limit of vanishing scalar charge.

For the tensor flux we obtain

$$\begin{aligned}
\mathcal{F}_T = & \frac{8}{15} \frac{\eta^2}{G\alpha^2} \left(\frac{G\alpha M}{r} \right)^4 \left\{ (12v^2 - 11\dot{r}^2) \right. \\
& + \frac{1}{28} \left[-16 \left(170 - 10\eta + 63\bar{\gamma} + 84\beta_+ - 84 \frac{\Delta M}{M} \beta_- \right) v^2 \frac{G\alpha M}{r} \right. \\
& + (785 - 852\eta + 336\bar{\gamma}) v^4 - 2(1487 - 1392\eta + 616\bar{\gamma}) v^2 \dot{r}^2 + 3(687 - 620\eta + 280\bar{\gamma}) \dot{r}^4 \\
& \left. \left. + 8 \left(367 - 15\eta + 140\bar{\gamma} + 168\beta_+ - 168 \frac{\Delta M}{M} \beta_- \right) \dot{r}^2 \frac{G\alpha M}{r} + 16(1 - 4\eta) \left(\frac{G\alpha M}{r} \right)^2 \right] \right\} \\
& + \frac{48G^3 M \alpha \mu}{5r^8} \left(100\dot{r}^4 - 105\dot{r}^2 v^2 + 15v^4 + 18 \frac{GM\alpha}{r} \dot{r}^2 - 11 \frac{GM\alpha}{r} v^2 \right) \bar{\zeta}_2 - \frac{64G^4 M^2 \alpha^3 \mu^2}{15r^7} (7\dot{r}^2 - 6v^2) \zeta_1 \\
& - \frac{192G^4 M^2 \alpha^3 \mu^2}{5r^9} (4\dot{r}^2 - 3v^2) \zeta_2. \tag{B13}
\end{aligned}$$

Specializing to circular orbits and expressing the results in terms of x leads to

$$\mathcal{F}_T(x) = x^5 [T5 + x (T6 + T6_{\text{tid},1} x^2 + T6_{\text{tid},2} x^4)], \tag{B14}$$

with the coefficients given by

$$\begin{aligned}
T5 &= \frac{32\eta^2}{5\alpha^2 G}, \\
T6 &= \left(\frac{2\eta^2}{105\alpha^2 G} \right) \left(-1247 - 448\bar{\gamma} + 896\frac{\Delta M}{M}\beta_- - 896\beta_+ - 980\eta \right), \\
T6_{\text{tid},1} &= \frac{256\mu^2\zeta_1}{15\alpha^4 G^3 M^5}, \\
T6_{\text{tid},2} &= \left(\frac{192\mu\tilde{\zeta}_2}{5\alpha^7 G^5 M^7} + \frac{384\mu^2\zeta_2}{5\alpha^6 G^5 M^7} \right).
\end{aligned} \tag{B15}$$

c. GW phase evolution

In Sec. [IV E](#) we discuss the derivation of the DD and QD Fourier phase as a function of frequency. In the DD

domain the ratio obtained from energy balance in [\(4.32\)](#) is expanded as [\(4.34\)](#) with coefficients

$$\begin{aligned}
E'_0 &= -\frac{3}{2} - \frac{\eta}{6} - \frac{4\bar{\gamma}}{3} + \frac{4}{3} \left(\beta_+ - \frac{\Delta M}{M}\beta_- \right) - x^2 \frac{20\zeta_1}{3G^2\alpha^2 M^3} - x^4 \frac{54\zeta_2}{G^4\alpha^4 M^5}, \\
f_2^{DD} &= \frac{24}{5\alpha S_-^2} + \frac{4S_+^2}{5S_-^2} - \frac{4\beta_+}{3} + \frac{4\beta_- \Delta M}{3M} - \frac{14}{5} - \frac{4\eta}{3} - \frac{2\bar{\gamma}}{3} + \frac{4\beta_- S_+}{\bar{\gamma} S_-} - \frac{4\beta_+ \Delta M S_+}{\bar{\gamma} M S_-} + \frac{4\beta_+}{\bar{\gamma}} - \frac{4\beta_- \Delta M}{\bar{\gamma} M} \\
&\quad + x^2 \left(-\frac{\bar{\zeta}_1}{G^2 M^3 \alpha^{7/2} S_- \mu} + \frac{4\zeta_1}{3G^2 \alpha^2 M^3} \right) + x^4 \frac{6\zeta_2}{G^4 \alpha^4 M^5}.
\end{aligned} \tag{B16}$$

The total DD phase within our approximations is given by

$$\psi_{DD} = \frac{1}{4\eta S_-^2 x^{3/2}} \left\{ 1 + \rho^{\text{DD}} x + x^3 \left[\rho_{\text{tid}}^{\text{DD}} \log(x) - \frac{2}{3} \rho_{\text{tid}}^{\text{DD}} \right] - \frac{270\zeta_2}{7\alpha^4 G^4 M^5} x^5 \right\} + \phi_c - 2\pi f t_c, \tag{B17}$$

with

$$\rho^{\text{DD}} = -\frac{108}{5\alpha S_-^2} + 12 \left(\beta_+ - \frac{\Delta M}{M}\beta_- \right) - \frac{9}{4\alpha^{3/2} M S_-} (\Delta M q_B \beta_A - M q_B \beta_A + \Delta M q_A \beta_B + M q_A \beta_B) \tag{B18}$$

$$+ \frac{18}{\bar{\gamma}} \frac{S_+}{S_-} \left(\frac{\Delta M}{M}\beta_+ - \beta_- \right) - 3\bar{\gamma} + \frac{21\eta}{4} - \frac{18S_+^2}{5S_-^2} + \frac{117}{20}, \tag{B19}$$

$$\rho_{\text{tid}}^{\text{DD}} = \frac{3}{G^2 \alpha^2 M^3 \eta} \left[-\frac{\bar{\zeta}_1}{\alpha^{3/2} M S_-} + 16\eta\zeta_1 \right]. \tag{B20}$$

In the QD domain, the energy balance ratio is expanded as [\(4.41\)](#) with coefficients given by

$$\begin{aligned}
f_2^{nd} &= \frac{1}{\xi} \left[-\frac{8\beta_+}{3} - \frac{4\bar{\gamma}}{3} - \frac{35\eta}{12} + \frac{8\beta_- \Delta M}{3M} - \frac{1247}{336} + x^2 \frac{8\zeta_1}{3G^2 \alpha^2 M^3} + x^4 \left(\frac{6\tilde{\zeta}_2}{G^4 \alpha^5 M^5} + \frac{12\zeta_2}{G^4 \alpha^4 M^5} \right) \right], \\
f^d &= -\frac{4\beta_+}{3} + \frac{4\beta_- \Delta M}{3M} - \frac{14}{5} - \frac{4\eta}{3} - \frac{2\bar{\gamma}}{3} + \frac{4\beta_- S_+}{\bar{\gamma} S_-} - \frac{4\beta_+ \Delta M S_+}{\bar{\gamma} M S_-} + \frac{4\beta_+}{\bar{\gamma}} - \frac{4\beta_- \Delta M}{\bar{\gamma} M} \\
&\quad + x^2 \left(-\frac{\bar{\zeta}_1}{G^2 \alpha^{7/2} M^3 S_- \mu} + \frac{4\zeta_1}{3G^2 \alpha^2 M^3} \right) + x^4 \frac{6\zeta_2}{G^4 \alpha^4 M^5}.
\end{aligned} \tag{B21}$$

The quadrupolar driven phase evolution is given by

$$\psi^{\text{QD}} = \psi_{\text{non-dip}} + \psi_{\text{dip}} + \phi_c + 2\pi f t_c, \tag{B22}$$

with

$$\psi_{\text{non-dip}} = \frac{3\alpha}{128\eta\xi x^{5/2}} \left[1 + \rho^{nd} x + \rho_{\text{tid}}^{nd,1} x^3 + \rho_{\text{tid}}^{nd,2} x^5 \right], \tag{B23a}$$

$$\psi_{\text{dip}} = -\frac{5S_{\pm}^2\alpha^2}{1792\eta\xi^2x^{7/2}} \left[1 + \rho^d x + \rho_{\text{tid}}^{d,1} x^3 - \frac{280\zeta_1}{3\alpha^2 G^2 M^3 \xi} \right], \quad (\text{B25b})$$

$$+ \rho_{\text{tid}}^{d,2} x^5 \log(x) - \frac{2}{3} \rho_{\text{tid}}^{d,2} x^5 \Big], \quad (\text{B23b}) \quad \rho_{\text{tid}}^{d,2} = -\frac{140\tilde{\zeta}_2}{\alpha^5 G^4 M^6 \eta \xi} - \frac{560\zeta_2}{\alpha^4 G^4 M^5} - \frac{280\zeta_2}{\alpha^4 G^4 M^5 \xi}. \quad (\text{B25c})$$

and $\xi = 1 + S_{\pm}^2\alpha/6$. The non-dipolar coefficients are

$$\rho^{nd} = \frac{6235}{756\xi} - \frac{10}{3} - \left(10 - \frac{175}{\xi}\right) \frac{\eta}{27} + \frac{80}{27} \left(\frac{1}{\xi} - 1\right) \bar{\gamma} + \left(\frac{80}{27} + \frac{160}{27\xi}\right) \left(\beta_+ - \frac{\Delta M}{M} \beta_-\right), \quad (\text{B24a})$$

$$\rho_{\text{tid}}^{nd,1} = \frac{400\zeta_1}{3\alpha^2 G^2 M^3} + \frac{160\zeta_1}{3\alpha^2 G^2 M^3 \xi}, \quad (\text{B24b})$$

$$\rho_{\text{tid}}^{nd,2} = -\frac{24\tilde{\zeta}_2}{\alpha^5 G^4 M^6 \eta \xi} - \frac{216\zeta_2}{\alpha^4 G^4 M^5} - \frac{48\zeta_2}{\alpha^4 G^4 M^5 \xi}, \quad (\text{B24c})$$

and the dipolar parts are

$$\rho^d = \frac{1247}{96\xi} - \frac{301}{40} + \left(\frac{245}{24\xi} - \frac{21}{8}\right) \eta + \left(\frac{14}{3\xi} - \frac{7}{2}\right) \bar{\gamma} + \frac{7S_+}{\bar{\gamma}S_-} \left(\beta_- - \frac{\Delta M}{M} \beta_+\right) + \left(\frac{28}{3\xi} + \frac{7}{\bar{\gamma}}\right) \left(\beta_+ - \frac{\Delta M}{M} \beta_-\right), \quad (\text{B25a})$$

$$\rho_{\text{tid}}^{d,1} = -\frac{35\bar{\zeta}_1}{2\alpha^{7/2} G^2 M^4 S_- \eta} - \frac{280\zeta_1}{3\alpha^2 G^2 M^3}$$

Appendix C: Ready-to-use expressions for the tidal coefficients in the phase

For practical purposes, it is useful to study the combinations of tidal deformabilities and masses that appear in the GW phase with different powers of x . Here, we give explicit expressions for these terms.

1. Quadrupolar-driven regime

The general structure of the tidal contribution to the phase in the QD regime was given in (4.44). Here, we provide the coefficients explicitly in terms of the NS properties.

The coefficient c_2 arising from dipolar tidal terms contributing to the dipolar piece of the phase read

$$c_2 = \frac{25}{3\alpha^2 G^2 M^3 \xi^3} \left\{ \left[\frac{4}{3}(\xi + 1)M_B q_B S_- + \frac{1}{4}\sqrt{\alpha\xi}M \right] q_B \frac{\lambda_A^{S,\ell=1}}{M_A} + \left[\frac{4}{3}(\xi + 1)M_A q_A S_- - \frac{1}{4}\sqrt{\alpha\xi}M \right] q_A \frac{\lambda_B^{S,\ell=1}}{M_B} \right\}, \quad (\text{C1})$$

where the parameters α , and ξ were defined in (3.7), and (4.39) with (4.23), respectively. As this parameter (C1) is multiplied by S_- in the phase (4.44), in case of identical NSs where $S_- = 0$ it does not contribute.

Next, the parameter c_3 arising from the contribution of scalar dipolar tidal effects to the non-dipolar part of the Fourier phase is given by

$$c_3 = \frac{140}{3\alpha^3 \xi^2} \left[\underbrace{\frac{4}{G^2 M^3} \left(M_B q_B^2 \frac{\lambda_A^{S,\ell=1}}{M_A} + M_A q_A^2 \frac{\lambda_B^{S,\ell=1}}{M_B} \right)}_{\rightarrow q^2 \Lambda_S^{\ell=1} \text{ for } M_A=M_B} + \frac{5}{42} \frac{(q_A + q_B)^2}{G^2 M^3} \left(M_B q_B^2 \frac{\lambda_A^{S,\ell=1}}{M_A} + M_A q_A^2 \frac{\lambda_B^{S,\ell=1}}{M_B} \right) \right], \quad (\text{C2})$$

and its value for identical NSs was given in (4.46).

Effects that involve all three Love numbers first appear in the quadrupolar tidal contributions to the dipolar piece of the phase, through the coefficient

$$c_4 = \frac{50}{3\alpha^4 G^4 M^5 \xi^3} \left\{ [2(2\xi + 1)M_B + \alpha M] \frac{\lambda_A^T}{M_A} + [2(2\xi + 1)M_A + \alpha M] \frac{\lambda_B^T}{M_B} \right\} - \frac{50}{3\alpha^4 G^4 M^5 \xi^3} \left\{ [4(2\xi + 1)M_B + \alpha M] \frac{\lambda_A^{ST}}{M_A} + [4(2\xi + 1)M_A + \alpha M] \frac{\lambda_B^{ST}}{M_B} \right\} + \frac{100(2\xi + 1)}{3\alpha^4 G^4 M^5 \xi^3} \left(M_B q_B^2 \frac{\lambda_A^{S,\ell=2}}{M_A} + M_A q_A^2 \frac{\lambda_B^{S,\ell=2}}{M_B} \right), \quad (\text{C3})$$

where λ^T and λ^{ST} are understood to be the quadrupolar $\ell = 2$ results, which is their lowest nontrivial multipolar order. Similarly to c_2 , the coefficient (C3) also appears multiplied by S_- in the phase (4.44) and thus does not contribute in the equal-mass limit.

The coefficient of x^5 in (4.44) likewise has contributions from all three kinds of tidal deformabilities and is given by

$$c_5 = \frac{39}{2\alpha^5\xi^2} \left(\frac{7}{26} \frac{32(q_A + q_B)^2}{7G^4M^5} \underbrace{\left[\left(\frac{3M_B}{8} + \eta_q M \right) \frac{\lambda_A^T}{M_A} + \left(\frac{3M_A}{8} + \eta_q M \right) \frac{\lambda_B^T}{M_B} \right]}_{\rightarrow q^2 \Lambda_T^{\ell=2} \text{ for } M_A=M_B} + \frac{16}{26G^4(M\alpha)^5\xi^2} \left\{ [2(9\xi + 2)M_B + \alpha M] q_B \frac{\lambda_A^{ST}}{M_A} + [2(9\xi + 2)M_A + \alpha M] q_A \frac{\lambda_B^{ST}}{M_B} \right\} - \frac{16(9\xi + 2)}{13G^4(M\alpha)^5\xi^2} \left[q_B M_B \frac{\lambda_A^S}{M_A} + q_A M_A \frac{\lambda_B^S}{M_B} \right] \right), \quad (\text{C4})$$

where again λ^T , λ^{ST} and λ^S are understood to be quadrupolar $\ell = 2$. We have defined the symmetric charge ratio

$$\eta_q = \frac{q_A q_B}{(q_A + q_B)^2}. \quad (\text{C5})$$

For two identical bodies, the result (C4) reduces to (4.47).

2. Dipolar-driven regime

Similarly to the quadrupolar-driven phase, the dipolar-driven phase can be rewritten as

$$\psi_{DD} = \frac{1}{4\eta x^{3/2}} \left\{ (\text{pp}) + c_3^{DD} \left(\log x - \frac{2}{3} \right) x^3 + c_5^{DD} x^5 \right\}, \quad (\text{C6})$$

with c_3^{DD} and c_5^{DD} given by

$$c_3^{DD} = - \frac{1}{G^2 M^3 \alpha^4 S_-^3} \left[(8M_B q_B - \sqrt{\alpha} M) q_B \frac{\lambda_A^{S,\ell=1}}{M_A} + (8M_A q_A + \sqrt{\alpha} M) q_A \frac{\lambda_B^{S,\ell=1}}{M_B} \right], \quad (\text{C7})$$

$$c_5^{DD} = - \frac{90}{7\alpha^6 G^4 M^5 S_-^2} \left[\frac{M_B}{M_A} \left(q_B^2 \lambda_A^{S,\ell=2} - 2q_B \lambda_A^{ST,\ell=2} + \lambda_A^{T,\ell=2} \right) + \frac{M_A}{M_B} \left(q_A^2 \lambda_B^{S,\ell=2} - 2q_A \lambda_B^{ST,\ell=2} + \lambda_B^{T,\ell=2} \right) \right]. \quad (\text{C8})$$

For a system of two identical NSs, the scalar flux vanishes and there is no dipolar-driven phase.

Appendix D: Gravitational waves in Jordan frame from Einstein frame results

In this appendix, we provide details on the relation of GWs in the Jordan frame to those in the Einstein frame that was briefly stated in Sec. IV C. While this topic has already been discussed in the literature, e.g. [63, 82, 83], we generalize the results to arbitrary coupling functions

and, in Sec. D 2 a result valid beyond the short-wave limit for describing GWs.

1. Derivation based on the short-wave approximation

a. Geodesic deviation and linearized frame transformations

In analyzing the basic physics of GW detection, it is useful to consider the deviation between geodesics of nearby test masses due to curvature induced by GWs. Our aim is to use this together with the frame transformations (2.2) to relate the Einstein-frame metric perturbations to physical effects on test masses in the Jordan frame.

In brief (see e.g. the review [97] for more details and [82] for the application to ST theories), we assume that one geodesic is at $z^\alpha(\tau)$, where τ is proper time, and a nearby one is at $z^\alpha(\tau) + L^\alpha(\tau)$, where L^α is small. The geodesic deviation in the Jordan frame is given by

$$\frac{D_*^2}{d\tau^2} L^\mu = R_{\alpha\nu\beta}^\mu u^\alpha u^\beta L^\nu, \quad (\text{D1})$$

where $D_*/d\tau$ denotes the total derivative along the worldline. In the local proper detector frame, this reduces to

$$\ddot{L}^i = -R_{*0j0}^i L^j = \frac{1}{2} \ddot{h}_{ij}^* L^j, \quad (\text{D2})$$

with h_{ij}^* the spatial parts of a small metric perturbation around a background metric $\eta_{\mu\nu}^*$

$$g_{\mu\nu}^* = \eta_{\mu\nu}^* + h_{\mu\nu}^*, \quad g_{\mu\nu} = \eta_{\mu\nu} + h_{\mu\nu}, \quad (\text{D3a})$$

where we have also written down the expansion of the metric in the Einstein frame. We recall that in the Einstein frame, vacuum gravity behaves as in GR and the spacetime of a compact binary source is asymptotically Minkowski, with $\eta_{\mu\nu}$ the standard Minkowski metric. Similarly to (D3), we expand the scalar fields for small fluctuations around their asymptotic background values

$$\phi = \phi_0 + \delta\phi, \quad |\delta\phi| \ll \phi_0, \quad (\text{D3b})$$

and likewise for the Einstein-frame field φ . Next, substituting (D3) into the conformal transformation (2.2) and expanding to first order in the small quantities yields the relation [98]

$$h_{\mu\nu}^* = A_0^2 \left(h_{\mu\nu} + 2 \frac{A_0'}{A_0} \delta\varphi \eta_{\mu\nu} \right), \quad (\text{D4})$$

where the subscript 0 denotes evaluation of the function at φ_0 . Using (D4) to compute the Riemann tensor yields

$$R_{*0j0}^k = - \frac{1}{A_0^2} \eta^{ki} \frac{1}{2} \ddot{h}_{ij}. \quad (\text{D5})$$

Taking two time derivatives of (D4) leads to

$$\ddot{h}_{ij}^* \simeq A_0^2 \left(\ddot{h}_{ij} + \frac{2A_0'}{A_0} \delta\ddot{\varphi} \eta_{ij} \right), \quad (\text{D6})$$

at first order in the perturbations and at leading order in the distance to the source, i.e. we neglect terms such as $\dot{\varphi}_0 \delta\varphi$. Substituting this into (D5) yields

$$R_{*0j0}^i \simeq - \frac{1}{2} \left(\ddot{h}_{ij} + \frac{2A_0'}{A_0} \delta\ddot{\varphi} \eta_{ij} \right). \quad (\text{D7})$$

Comparing with (D2), we can redefine the Jordan frame metric perturbation as

$$\ddot{h}_{ij}^J \equiv \frac{\ddot{h}_{ij}^*}{A_0^2} = \ddot{h}_{ij} + \frac{2A_0'}{A_0} \delta\ddot{\varphi} \eta_{ij}. \quad (\text{D8})$$

At first glance, one might think that there is a clash between (D6) and (D8) due to the factor of A_0^2 . This is because (D2) does not contain any information about the frame transformations. In particular, the quantity (D8) is the relevant one for geodesic deviation in our approximations.

b. Reduction to physical degrees of freedom

The next step is to fix a gauge in which only the physical degrees of freedom remain, such as the TT gauge in GR. We start by applying the transverse projector (4.26) on both sides of (D8),

$$\ddot{h}_{ij}^{J,T} \simeq \ddot{h}_{ij}^T + \frac{2A_0'}{A_0} \delta\ddot{\varphi} (\delta_{ij} - N_i N_j), \quad (\text{D9})$$

where T stands for transverse, we have used that $\eta_{ij}^{*T} = P_i^k \eta_{km}^* P_j^M = P_{ij}$ and substituted (4.26). Taking the trace-less part yields

$$\ddot{h}_{ij}^{J,TT} \simeq \ddot{h}_{ij}^{TT}. \quad (\text{D10})$$

This shows explicitly that the tensor plus and cross GW polarizations are the same in both frames. This also follows from expanding $\delta_{ij}^\mu = g_{ij}^\mu = g_{ij}^{*\mu}$ with (D3) to linear order in the perturbations, which likewise yields $h_j^i = h_j^{*i}$. As shown in [82], we can replace the term \ddot{h}_{ij}^{*T} in (D9) by \ddot{h}_{ij}^{*TT} . For the coupling $A(\varphi) = \varphi^{1/2}$ in (D9), this reproduces the result in [63, 83, 99] with the redefinition $\Psi = \delta\varphi/\varphi_0$.

In summary, the Jordan-frame gravitational radiation can be computed from the Einstein-frame quantities via

$$h_{ij}^{J,T} \simeq h_{ij}^{TT} + \frac{2A_0'}{A_0} \delta\varphi (\delta_{ij} - N_i N_j), \quad (\text{D11})$$

where for the setting considered here, h_{ij}^{TT} is the waveform computed in Sec. IV B and given explicitly by (B9), and $\delta\varphi$ the scalar waveform computed in Sec. IV A and given explicitly in (B7).

c. Polarization components

We next use the expansion (D3) together with (2.4) to express the contribution of the Einstein frame scalar field in terms of the Jordan frame one,

$$- \frac{2A_0'}{A_0} \delta\ddot{\varphi} = \frac{F'}{F\sqrt{\Delta}} \Big|_0 \delta\ddot{\varphi} \simeq \frac{F'(\phi_0)}{F(\phi_0)} \delta\ddot{\phi}. \quad (\text{D12})$$

Using this in the result for the metric perturbation (D11), the decomposition into the fundamental polarization components discussed in [82] applies. This shows that in addition to the plus and cross tensorial polarizations, there is also a scalar mode. As discussed in [82], for theories with a coupling to the Ricci scalar of the form $F(\phi) = \phi$ in (2.1) and wave propagation in the z -direction

$$h_{ij}^J |_{F(\phi)=\phi} = h_+ e_{ij}^{(+)} + h_\times e_{ij}^{(\times)} - \frac{\delta\phi}{\phi_0} e_{ij}^S, \quad (\text{D13})$$

with the amplitude of the scalar polarization obtained by using (D12) together with the identification of $\delta\varphi$ as the scalar radiation field in the Einstein frame computed in Sec. IV A.

d. Asymptotic flatness and size of the scalar GWs in the Jordan frame

From the expressions derived above, we can draw several interesting conclusions. The first is regarding the asymptotic background metric $\eta_{\mu\nu}^*$ that appears in (D3). From the frame transformation (2.2), it follows that

that $\eta_{\mu\nu}^* = A(\varphi_0)^2 \eta_{\mu\nu}$, with $\eta_{\mu\nu}$ the Minkowski metric. The transformation indicates that in general, the Jordan frame metric is not asymptotically flat. There are two ways to avoid this difficulty: one is to rescale the coordinates to absorb the factor A_0^2 , such that the line element ds_*^2 in the Jordan frame is indeed the correct flat-space one [16, 45]; another way is to rescale the conformal factor such that $A(\varphi) \rightarrow A(\varphi)/A(\varphi_0)$, or equivalently imposing $A(\varphi_0) = 1$, for which no redefinition is necessary.

A second interesting point is that due to the scalar-field contribution, the metric perturbation in the Jordan frame is only transverse but not traceless. However, depending on the coupling function, the scalar contribution to the waveform (D8) can be strongly suppressed, due to the factor of $A'(\varphi_0)/A(\varphi_0)$. For instance, for theories with generic power law couplings $A(\varphi) = \varphi^\kappa$, dilatonic couplings $A(\varphi) = e^{\gamma\varphi}$, or Gaussian couplings [20] $A(\varphi) = e^{\frac{1}{2}\beta_0\varphi^2}$, depending on the coupling constants and values of $\varphi_0 = \varphi_\infty$, the scalar field contribution to the Jordan-frame waveform may be suppressed by many orders of magnitude.

2. Derivation beyond the short-wave approximation

The results in Sec. D1 above can be applied to ground-based detectors as long as the size of the arms L is shorter than the reduced GW wavelength $\tilde{\lambda}$, $L \ll \tilde{\lambda}$. To study GWs beyond this approximation requires analyzing the scattering of light between mirrors as we now discuss. Similarly to (D1), the time it takes for the light of the interferometer to scatter from the mirror and come back, is given by the same expression as in GR, with their corresponding metrics. We will proceed as above and start from the physical Jordan frame, and at the end rewrite the expressions in terms of Einstein frame quantities. Similarly to [100], we consider the plus polarization of a gravitational wave moving along the z -axis. We will focus on two different kinds of orientations for the interferometer arms, when they lie along the x - y or the x - z plane.

In this set-up, we have

$$ds^2 = -dt^2 + [1 + h_+ + \Phi]dx^2 + [1 - h_+ + \Phi]dy^2 + dz^2, \quad (\text{D14})$$

with Φ defined in (D13). For null rays, $ds^2 = 0$ and, at first order in h_+ and Φ , for the x -arm,

$$dx = \pm \left\{ 1 - \frac{1}{2} [h_+ + \Phi] \right\} dt. \quad (\text{D15})$$

For a photon travelling from the origin $(x, t) = (0, t_0)$ to the mirror at $(x, t) = (L_x, t_1)$, we integrate (D15) with the plus sign. For the return trip, from $(x, t) = (L_x, t_1)$ to $(x, t) = (0, t_2)$, we use the minus sign.

The time it takes for a photon to complete N round trips along the x -arm is given, at first order in the perturbations, by

$$\begin{aligned} \Delta t^{(x)} &= N(t_2 - t_0) \\ &= 2NL_x + \frac{N}{2} \int_{t_0}^{t_0+2L_x} [h_+(t') + \Phi(t')] dt', \end{aligned} \quad (\text{D16})$$

where we have substituted $t_2 = t_0 + 2L_x + \mathcal{O}(h_+, \Phi)$ in the upper limit of the integral. Considering a plane wave as a simple example,

$$h_+ = A^+ \cos(\omega_{\text{gw}} t), \quad \Phi = \Phi_0 \cos(\omega_s t), \quad (\text{D17})$$

with ω_{gw} and ω_s the frequency of the GW and the scalar field, respectively, and using

$$\int_{t_0}^{t_0+2L_x} \cos(\omega t) = \frac{\sin(\omega L_x)}{(\omega L_x)} \cos[\omega(t_0 + L_x)], \quad (\text{D18})$$

yields,

$$\begin{aligned} \Delta t^{(x)} &= 2NL_x \\ &\times \left\{ 1 + \frac{1}{2} \left[h_+(t_0 + L_x) + \Phi(t_0 + L_x) \frac{\omega_{\text{gw}}}{\omega_s} \frac{\sin(\omega_s L_x)}{\sin(\omega_{\text{gw}} L_x)} \right] \right. \\ &\quad \left. \times \frac{\sin(\omega_{\text{gw}} L_x)}{(\omega_{\text{gw}} L_x)} \right\}, \end{aligned} \quad (\text{D19})$$

or, considering that we observe the wave at some given time $t \equiv t_2 = t_0 + 2L_x$, yields

$$\begin{aligned} \Delta t^{(x)} &= 2NL_x \\ &\times \left\{ 1 + \frac{sc_{\text{gw},x}}{2} \left[h_+(t - L_x) + \Phi(t - L_x) \frac{sc_{s,x}}{sc_{\text{gw},x}} \right] \right\}, \end{aligned} \quad (\text{D20})$$

where we define

$$sc_{p,q} \equiv \text{sinc}(\omega_p L_q) = \frac{\sin(\omega_p L_q)}{(\omega_p L_q)}. \quad (\text{D21})$$

For the y -arm the result is similar but with $h_+ \rightarrow -h_+$. The phase-shift $\Delta\Theta$ produced in the interferometer is given by

$$\begin{aligned} \Delta\Theta^{(x-y)} &= \omega_L (\Delta t^{(x)} - \Delta t^{(y)}) \\ &= 2N\omega_L \Delta L \\ &\times \left\{ 1 + \frac{L^+}{2\Delta L} [h_+(t_+) sc_{\text{gw},+} + \Phi(t_+) sc_{s,+}] \right. \\ &\quad \left. + \frac{L^-}{2\Delta L} [h_+(t_-) sc_{\text{gw},-} - \Phi(t_-) sc_{s,-}] \right\}, \end{aligned} \quad (\text{D22})$$

with ω_L the laser frequency, and the definitions

$$\begin{aligned} L &\equiv \frac{L_x + L_y}{2}, \quad \Delta L \equiv L_x - L_y, \\ L^{+/-} &\equiv L \pm \frac{\Delta L}{2}, \quad t_{+/-} = t - L^\pm. \end{aligned} \quad (\text{D23})$$

For an interferometer with equal-length arms, $\Delta L = 0$, $L^+ = L^- = L$ and

$$\Delta\Theta^{(x-y)} = h_+(t-L)\Theta_{\text{arm}} \frac{\sin(\omega_{\text{gw}}L)}{(\omega_{\text{gw}}L)}, \quad (\text{D24})$$

with $\Theta_{\text{arm}} = 2LN\omega_L$. This is the same result as in GR. This is because the scalar field contributes equally in the x and y directions, and therefore its oscillations will cancel out.

We now focus on the case where the arms are in the x - z axis. In this case, the expression for the x -arm is the same as above, and for the z -axis we have

$$\Delta t^{(z)} = 2NL_z, \quad (\text{D25})$$

since the wave is propagating along the z axis and is transverse. In this case, there is no contribution of the scalar field along the z -axis and the phase yields

$$\begin{aligned} \Delta\Theta^{(x-z)} &= \omega_L \left(\Delta t^{(x)} - \Delta t^{(z)} \right) \\ &= 2N\omega_L \Delta L \\ &\quad \left\{ 1 + \frac{L^+}{2\Delta L} [h_+(t_+)sc_{\text{gw},+} + \Phi(t_+)sc_{s,+}] \right\}, \end{aligned} \quad (\text{D26})$$

with the change of label $y \rightarrow z$ in the definitions (D23). For the case that the arms have equal length, we obtain

$$\Delta\Theta^{(x-z)} = \frac{\Theta_{\text{arm}}}{2} [h_+(t-L)sc_{\text{gw},+} + \Phi(t-L)sc_{s,+}]. \quad (\text{D27})$$

Using (D11), in terms of the Einstein frame waveforms we have

$$\Delta\Theta^{(x-y)} = \Theta_{\text{arm}} h_+^*(t-L)sc_{\text{gw},+}, \quad (\text{D28})$$

$$\Delta\Theta^{(x-z)} = \frac{\Theta_{\text{arm}}}{2} [h_+^*(t-L)sc_{\text{gw},+} - 2\alpha_\infty \delta\varphi(t-L)sc_{s,+}]. \quad (\text{D29})$$

Note that the lengths and frequencies will be the same as long as we are far from the scalar field. In the short-wave approximation, $sc \rightarrow 1$ and we recover the result in [82] for the scalar field contribution.

Appendix E: Elaboration on the parameter space study

In Sec. VD 2 we did a phase space analysis of the tidal contributions to the QD Fourier phase captured by the

c_i coefficients in (4.44). Based on these parameter space studies we selected three types of systems that maximize the different types of tidal contributions and an intermediate scenario both for NS-NS and BH-NS systems. In this section in the main text we showed two of these parameter space plot explicitly in Fig. 7 for the sake of readability. In this appendix we elaborate on this analysis of Sec. VD 2, showing the parameter space results for the other coefficients in (4.44) in Fig. 10. In Fig 10 we show the contour plots for the different c_i coefficients defined in (4.44), in the (M_A, M_B) parameter space. We fix the SLy EoS, although the discussion is qualitatively similar for the WFF1 and H4 EoS.

The contour plots for the quadrupolar tensor tidal contributions captured in $(\frac{39}{2\alpha^5\epsilon^2}\tilde{\Lambda} + c_5)$ are for NS-NS and BH-NS systems qualitatively similar, in that the maximum absolute value is reached for the lowest masses. This is because the coefficients depend on the inverse of the total mass, which is maximum towards the limit of the lower NS mass of $1M_\odot$. Hence, our first choice of types of systems that would be interesting to study with respect to maximizing the quadrupolar tensor tidal contributions is that of the lowest possible mass for both NS-NS and BH-NS systems

$$(M_A, M_B)_1^{\text{NS-NS}} = (1M_\odot, 1M_\odot), \quad (\text{E1a})$$

$$(M_A, M_B)_1^{\text{BH-NS}} = (5M_\odot, 1M_\odot). \quad (\text{E1b})$$

The absolute value of the other contributions in (4.44) for both systems is peaked when one of the masses corresponds to that of the maximum charge $M_q \equiv M(q_{\text{max}})$, and the other mass corresponds to the lowest possible configuration. This can be interpreted as scalar-tensor effects being more noticeable as the charge is maximum, which indeed characterises the strength of the scalar field. Therefore, our second choice of systems will be

$$(M_A, M_B)_2^{\text{NS-NS}} = (1M_\odot, M_q), \quad (\text{E2a})$$

$$(M_A, M_B)_2^{\text{BH-NS}} = (5M_\odot, M_q). \quad (\text{E2b})$$

Additionally, for a NS-NS system, the c_3 contribution reaches moderate values when $M_A = M_B = M_q$. This can be explained with that this contribution contains the dipolar scalar tidal contribution in ζ_1 , which is maximum for an equal-mass system at the maximum charge (see Fig. 3). Additionally, the prefactors in front of the tidal deformabilities in the c_i contributions in (4.44) also depend on the scalar charges and are maximised for the equal-mass, maximum-charge configurations, contributing to an overall lower effect than when considering one of the companions with the lowest mass, for which $q \sim 0$. Finally, we will also choose an intermediate case where effects are moderate,

$$(M_A, M_B)_3^{\text{NS-NS}} = (1.1M_\odot, 1.2M_\odot), \quad (\text{E3a})$$

$$(M_A, M_B)_3^{\text{BH-NS}} = (8.9M_\odot, 1.2M_\odot), \quad (\text{E3b})$$

where we choose slightly different masses for the NS-NS system to avoid the vanishing of the term S_- in the phase.

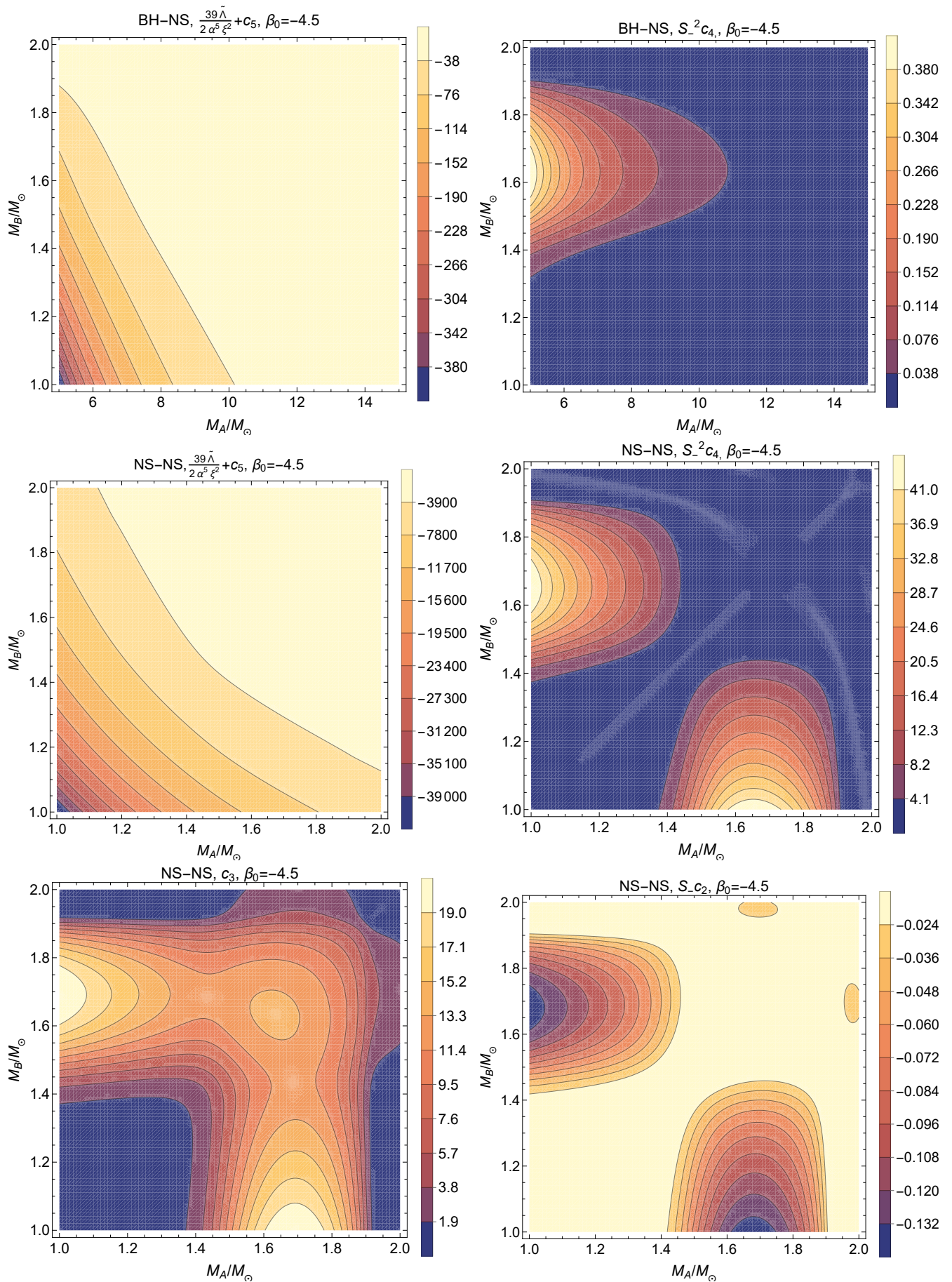


FIG. 10. Contour plots of the c_i coefficients defined in (4.44), in the $M_A - M_B$ parameter space for $\beta_0 = -4.5$ and the SLy EoS for a BH-NS system (top) and NS-NS system (middle and bottom). The plots for the other equations of state are qualitatively similar.

In the main body of the paper we refer to (E1a), (E2a) and (E3a) as scenarios 1, 2 and 3 respectively.

Appendix F: Dipolar Driven phase evolution

As discussed in Sec. VD 1 the DD domain for the parameter space of NS-NS and BH-NS systems we studied lies below the lower bound frequency of the groundbased detectors. However it might still be relevant to study the DD domain as the boundary frequency is an approximation and the transfer frequency regime might be a broader range extending to higher frequencies [49]. In this appendix we show the results of the tidal contributions to the DD Fourier phase (B17) in Fig. 11. The dipolar driven regime is not present for equal mass systems for which $S_- = 0$, so only Scenario 2 and 3 are non-trivial. The contributions are shown for frequencies 10^{-5} Hz to the boundary frequency (4.33). We choose to show here the different tidal contributions per Scenario instead of the contribution for the different systems; as in the DD regime the boundary frequency changes for different systems hence it is clearer to show the results per system. We find that the quadrupolar contributions are for both scenario's much smaller than in the QD regime. The dipolar scalar tidal contributions are clearly dominating which is expected in the DD domain where the dipolar radiation dominates over the quadrupole terms. The largest dipolar tidal contribution is found in Scenario 2, becoming of order 1 near the boundary frequency.

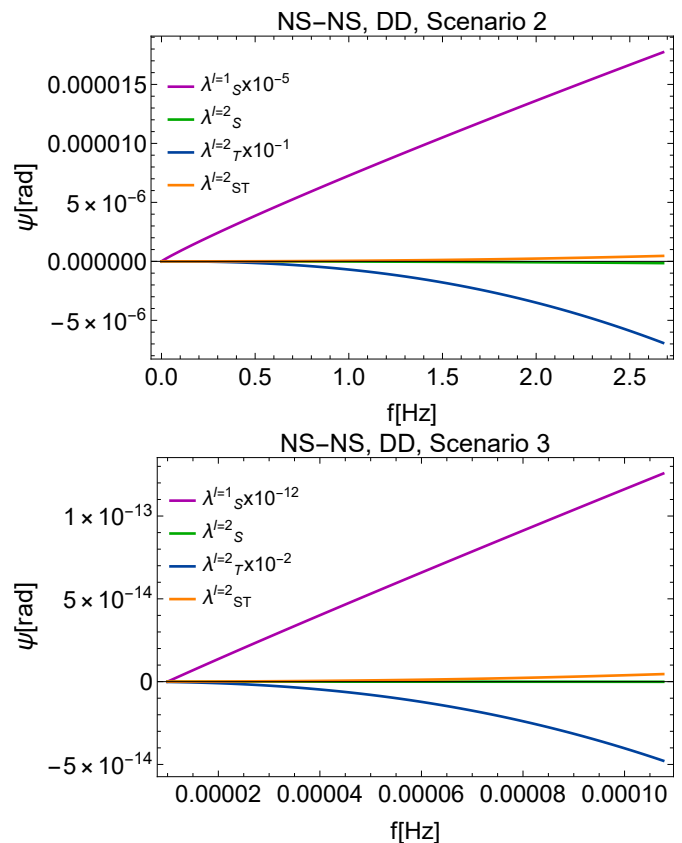


FIG. 11. Different contributions of the tidal deformabilities to the Fourier phase for a NS-NS system in the DD regime for the scenario 2 and 3 in Sec. II. Note that some of the contributions divided by orders of 10 to show the curves properly in one figure. The frequency domain is cut off at the boundary frequency of the DD domain (4.33).

-
- [1] B. P. Abbott *et al.* (LIGO Scientific, Virgo), GWTC-1: A Gravitational-Wave Transient Catalog of Compact Binary Mergers Observed by LIGO and Virgo during the First and Second Observing Runs, *Phys. Rev. X* **9**, 031040 (2019), [arXiv:1811.12907 \[astro-ph.HE\]](#).
 - [2] R. Abbott *et al.* (LIGO Scientific, Virgo), GWTC-2: Compact Binary Coalescences Observed by LIGO and Virgo During the First Half of the Third Observing Run, *Phys. Rev. X* **11**, 021053 (2021), [arXiv:2010.14527 \[gr-qc\]](#).
 - [3] R. Abbott *et al.* (KAGRA, VIRGO, LIGO Scientific), GWTC-3: Compact Binary Coalescences Observed by LIGO and Virgo during the Second Part of the Third Observing Run, *Phys. Rev. X* **13**, 041039 (2023), [arXiv:2111.03606 \[gr-qc\]](#).
 - [4] B. P. Abbott *et al.* (LIGO Scientific, Virgo), GW170817: Observation of Gravitational Waves from a Binary Neutron Star Inspiral, *Phys. Rev. Lett.* **119**, 161101 (2017), [arXiv:1710.05832 \[gr-qc\]](#).
 - [5] B. P. Abbott *et al.* (LIGO Scientific, Virgo), GW170817: Measurements of neutron star radii and equation of state, *Phys. Rev. Lett.* **121**, 161101 (2018), [arXiv:1805.11581 \[gr-qc\]](#).
 - [6] R. Abbott *et al.* (LIGO Scientific, KAGRA, VIRGO), Observation of Gravitational Waves from Two Neutron Star–Black Hole Coalescences, *Astrophys. J. Lett.* **915**, L5 (2021), [arXiv:2106.15163 \[astro-ph.HE\]](#).
 - [7] R. Abbott *et al.* (LIGO Scientific, VIRGO, KAGRA), Tests of General Relativity with GWTC-3, (2021), [arXiv:2112.06861 \[gr-qc\]](#).
 - [8] R. Alves Batista *et al.*, EuCAPT White Paper: Opportunities and Challenges for Theoretical Astroparticle Physics in the Next Decade, (2021), [arXiv:2110.10074 \[astro-ph.HE\]](#).
 - [9] A. Aprahamian *et al.*, Reaching for the horizon: The 2015 long range plan for nuclear science, (2015).

- [10] A. Bracco, The NuPECC long range plan 2017: perspectives in nuclear physics, *Europhysics News* **48**, 21 (2017).
- [11] B. P. Abbott *et al.* (LIGO Scientific, Virgo), Tests of general relativity with GW150914, *Phys. Rev. Lett.* **116**, 221101 (2016), [Erratum: *Phys.Rev.Lett.* 121, 129902 (2018)], arXiv:1602.03841 [gr-qc].
- [12] B. P. Abbott *et al.* (LIGO Scientific, Virgo), Tests of General Relativity with the Binary Black Hole Signals from the LIGO-Virgo Catalog GWTC-1, *Phys. Rev. D* **100**, 104036 (2019), arXiv:1903.04467 [gr-qc].
- [13] R. Abbott *et al.* (LIGO Scientific, Virgo), Tests of general relativity with binary black holes from the second LIGO-Virgo gravitational-wave transient catalog, *Phys. Rev. D* **103**, 122002 (2021), arXiv:2010.14529 [gr-qc].
- [14] Y. Fujii and K. Maeda, *The scalar-tensor theory of gravitation*, Cambridge Monographs on Mathematical Physics (Cambridge University Press, 2007).
- [15] T. Damour and G. Esposito-Farèse, Tensor-scalar gravity and binary-pulsar experiments, *Physical Review D* **54**, 1474–1491 (1996).
- [16] P. Pani and E. Berti, Slowly rotating neutron stars in scalar-tensor theories, *Phys. Rev. D* **90**, 024025 (2014), arXiv:1405.4547 [gr-qc].
- [17] S. M. Brown, Tidal Deformability of Neutron Stars in Scalar-tensor Theories of Gravity, *Astrophys. J.* **958**, 125 (2023), arXiv:2210.14025 [gr-qc].
- [18] T. Damour and G. Esposito-Farèse, Tensor multiscalar theories of gravitation, *Class. Quant. Grav.* **9**, 2093 (1992).
- [19] T. Damour and G. Esposito-Farèse, Gravitational wave versus binary - pulsar tests of strong field gravity, *Phys. Rev. D* **58**, 042001 (1998), arXiv:gr-qc/9803031.
- [20] T. Damour and G. Esposito-Farèse, Nonperturbative strong-field effects in tensor-scalar theories of gravitation, *Phys. Rev. Lett.* **70**, 2220 (1993).
- [21] D. D. Doneva, F. M. Ramazanoğlu, H. O. Silva, T. P. Sotiriou, and S. S. Yazadjiev, Spontaneous scalarization, *Rev. Mod. Phys.* **96**, 015004 (2024), arXiv:2211.01766 [gr-qc].
- [22] N. Andreou, N. Franchini, G. Ventagli, and T. P. Sotiriou, Spontaneous scalarization in generalised scalar-tensor theory, *Phys. Rev. D* **99**, 124022 (2019), [Erratum: *Phys.Rev.D* 101, 109903 (2020)], arXiv:1904.06365 [gr-qc].
- [23] G. Ventagli, *New Perspectives on Spontaneous Scalarization in Black Holes and Neutron Stars*, Ph.D. thesis, Nottingham U. (2022), arXiv:2209.15330 [gr-qc].
- [24] C. Palenzuela, E. Barausse, M. Ponce, and L. Lehner, Dynamical scalarization of neutron stars in scalar-tensor gravity theories, *Phys. Rev. D* **89**, 044024 (2014), arXiv:1310.4481 [gr-qc].
- [25] C. M. Will, The Confrontation between General Relativity and Experiment, *Living Rev. Rel.* **17**, 4 (2014), arXiv:1403.7377 [gr-qc].
- [26] P. C. C. Freire, N. Wex, G. Esposito-Farèse, J. P. W. Verbiest, M. Bailes, B. A. Jacoby, M. Kramer, I. H. Stairs, J. Antoniadis, and G. H. Janssen, The relativistic pulsar-white dwarf binary PSR J1738+0333 II. The most stringent test of scalar-tensor gravity, *Mon. Not. Roy. Astron. Soc.* **423**, 3328 (2012), arXiv:1205.1450 [astro-ph.GA].
- [27] D. Anderson, P. Freire, and N. Yunes, Binary pulsar constraints on massless scalar-tensor theories using Bayesian statistics, *Class. Quant. Grav.* **36**, 225009 (2019), arXiv:1901.00938 [gr-qc].
- [28] L. Shao, N. Sennett, A. Buonanno, M. Kramer, and N. Wex, Constraining nonperturbative strong-field effects in scalar-tensor gravity by combining pulsar timing and laser-interferometer gravitational-wave detectors, *Phys. Rev. X* **7**, 041025 (2017), arXiv:1704.07561 [gr-qc].
- [29] M. Kramer *et al.*, Strong-Field Gravity Tests with the Double Pulsar, *Phys. Rev. X* **11**, 041050 (2021), arXiv:2112.06795 [astro-ph.HE].
- [30] J. Zhao, P. C. C. Freire, M. Kramer, L. Shao, and N. Wex, Closing a spontaneous-scalarization window with binary pulsars, *Class. Quant. Grav.* **39**, 11LT01 (2022), arXiv:2201.03771 [astro-ph.HE].
- [31] E. Barausse, C. Palenzuela, M. Ponce, and L. Lehner, Neutron-star mergers in scalar-tensor theories of gravity, *Phys. Rev. D* **87**, 081506 (2013), arXiv:1212.5053 [gr-qc].
- [32] C. M. Will, Testing scalar - tensor gravity with gravitational wave observations of inspiraling compact binaries, *Phys. Rev. D* **50**, 6058 (1994), arXiv:gr-qc/9406022.
- [33] P. D. Scharre and C. M. Will, Testing scalar tensor gravity using space gravitational wave interferometers, *Phys. Rev. D* **65**, 042002 (2002), arXiv:gr-qc/0109044.
- [34] E. Berti, L. Gualtieri, M. Horbatsch, and J. Alsing, Light scalar field constraints from gravitational-wave observations of compact binaries, *Phys. Rev. D* **85**, 122005 (2012), arXiv:1204.4340 [gr-qc].
- [35] R. Niu, X. Zhang, B. Wang, and W. Zhao, Constraining Scalar-tensor Theories Using Neutron Star–Black Hole Gravitational Wave Events, *Astrophys. J.* **921**, 149 (2021), arXiv:2105.13644 [gr-qc].
- [36] H. Takeda, S. Tsujikawa, and A. Nishizawa, Gravitational-wave constraints on scalar-tensor gravity from a neutron star and black-hole binary GW200115, *Phys. Rev. D* **109**, 104072 (2024), arXiv:2311.09281 [gr-qc].
- [37] M. Quartin, S. Tsujikawa, L. Amendola, and R. Sturani, Constraining Horndeski theory with gravitational waves from coalescing binaries, *JCAP* **08**, 049, arXiv:2304.02535 [astro-ph.CO].
- [38] M. Shibata, K.-i. Nakao, and T. Nakamura, Scalar type gravitational wave emission from gravitational collapse in Brans-Dicke theory: Detectability by a laser interferometer, *Phys. Rev. D* **50**, 7304 (1994).
- [39] T. Harada, T. Chiba, K.-i. Nakao, and T. Nakamura, Scalar gravitational wave from Oppenheimer-Snyder collapse in scalar - tensor theories of gravity, *Phys. Rev. D* **55**, 2024 (1997), arXiv:gr-qc/9611031.
- [40] A. E. H. Love, The yielding of the earth to disturbing forces, *Proceedings of the Royal Society of London. Series A, Containing Papers of a Mathematical and Physical Character* **82**, 73 (1909).
- [41] T. Hinderer, Tidal Love numbers of neutron stars, *Astrophys. J.* **677**, 1216 (2008), [Erratum: *Astrophys.J.* 697, 964 (2009)], arXiv:0711.2420 [astro-ph].
- [42] E. E. Flanagan and T. Hinderer, Constraining neutron star tidal Love numbers with gravitational wave detectors, *Phys. Rev. D* **77**, 021502 (2008), arXiv:0709.1915 [astro-ph].
- [43] T. Damour and A. Nagar, Relativistic tidal properties of neutron stars, *Phys. Rev. D* **80**, 084035 (2009), arXiv:0906.0096 [gr-qc].

- [44] T. Binnington and E. Poisson, Relativistic theory of tidal Love numbers, *Phys. Rev. D* **80**, 084018 (2009), [arXiv:0906.1366 \[gr-qc\]](#).
- [45] G. Creci, T. Hinderer, and J. Steinhoff, Tidal properties of neutron stars in scalar-tensor theories of gravity, (2023), [arXiv:2308.11323 \[gr-qc\]](#).
- [46] T. Hinderer, B. D. Lackey, R. N. Lang, and J. S. Read, Tidal deformability of neutron stars with realistic equations of state and their gravitational wave signatures in binary inspiral, *Phys. Rev. D* **81**, 123016 (2010), [arXiv:0911.3535 \[astro-ph.HE\]](#).
- [47] S. Han and A. W. Steiner, Tidal deformability with sharp phase transitions in (binary) neutron stars, *Phys. Rev. D* **99**, 083014 (2019), [arXiv:1810.10967 \[nucl-th\]](#).
- [48] L. Bernard, Dipolar tidal effects in scalar-tensor theories, *Phys. Rev. D* **101**, 021501 (2020), [arXiv:1906.10735 \[gr-qc\]](#).
- [49] I. van Gemeren, B. Shiralilou, and T. Hinderer, Dipolar tidal effects in gravitational waves from scalarized black hole binary inspirals in quadratic gravity, (2023), [arXiv:2302.08480 \[gr-qc\]](#).
- [50] S. M. Brown, B. Krishnan, R. Somasundaram, and I. Tews, Can Neutron Star Tidal Effects Obscure Deviations from General Relativity?, (2024), [arXiv:2411.19129 \[gr-qc\]](#).
- [51] S. Ma, V. Varma, L. C. Stein, F. Foucart, M. D. Duez, L. E. Kidder, H. P. Pfeiffer, and M. A. Scheel, Numerical simulations of black hole-neutron star mergers in scalar-tensor gravity, *Phys. Rev. D* **107**, 124051 (2023), [arXiv:2304.11836 \[gr-qc\]](#).
- [52] K. Taniguchi, M. Shibata, and A. Buonanno, Quasiequilibrium sequences of binary neutron stars undergoing dynamical scalarization, *Phys. Rev. D* **91**, 024033 (2015), [arXiv:1410.0738 \[gr-qc\]](#).
- [53] M. Shibata, K. Taniguchi, H. Okawa, and A. Buonanno, Coalescence of binary neutron stars in a scalar-tensor theory of gravity, *Phys. Rev. D* **89**, 084005 (2014), [arXiv:1310.0627 \[gr-qc\]](#).
- [54] C. M. Will, Gravitational radiation from binary systems in alternative metric theories of gravity: dipole radiation and the binary pulsar., *ApJ* **214**, 826 (1977).
- [55] C. M. Will and H. W. Zaglauer, Gravitational Radiation, Close Binary Systems, and the Brans-Dicke Theory of Gravity, *ApJ* **346**, 366 (1989).
- [56] D. M. Eardley, Observable effects of a scalar gravitational field in a binary pulsar., *ApJ* **196**, L59 (1975).
- [57] T. Damour and G. Esposito-Farese, Testing gravity to second postNewtonian order: A Field theory approach, *Phys. Rev. D* **53**, 5541 (1996), [arXiv:gr-qc/9506063](#).
- [58] M. Saijo, H.-a. Shinkai, and K.-i. Maeda, Gravitational waves in Brans-Dicke theory : Analysis by test particles around a Kerr black hole, *Phys. Rev. D* **56**, 785 (1997), [arXiv:gr-qc/9701001](#).
- [59] M. Brunetti, E. Coccia, V. Fafone, and F. Fucito, Gravitational wave radiation from compact binary systems in the Jordan-Brans-Dicke theory, *Phys. Rev. D* **59**, 044027 (1999), [arXiv:gr-qc/9805056](#).
- [60] S. Mirshekari and C. M. Will, Compact binary systems in scalar-tensor gravity: Equations of motion to 2.5 post-Newtonian order, *Phys. Rev. D* **87**, 084070 (2013), [arXiv:1301.4680 \[gr-qc\]](#).
- [61] L. Bernard, Dynamics of compact binary systems in scalar-tensor theories: Equations of motion to the third post-Newtonian order, *Phys. Rev. D* **98**, 044004 (2018), [arXiv:1802.10201 \[gr-qc\]](#).
- [62] L. Bernard, Dynamics of compact binary systems in scalar-tensor theories: II. Center-of-mass and conserved quantities to 3PN order, *Phys. Rev. D* **99**, 044047 (2019), [arXiv:1812.04169 \[gr-qc\]](#).
- [63] R. N. Lang, Compact binary systems in scalar-tensor gravity. II. Tensor gravitational waves to second post-Newtonian order, *Phys. Rev. D* **89**, 084014 (2014), [arXiv:1310.3320 \[gr-qc\]](#).
- [64] N. Sennett, S. Marsat, and A. Buonanno, Gravitational waveforms in scalar-tensor gravity at 2PN relative order, *Phys. Rev. D* **94**, 084003 (2016), [arXiv:1607.01420 \[gr-qc\]](#).
- [65] R. N. Lang, Compact binary systems in scalar-tensor gravity. III. Scalar waves and energy flux, *Phys. Rev. D* **91**, 084027 (2015), [arXiv:1411.3073 \[gr-qc\]](#).
- [66] S. Ma and N. Yunes, Improved Constraints on Modified Gravity with Eccentric Gravitational Waves, *Phys. Rev. D* **100**, 124032 (2019), [arXiv:1908.07089 \[gr-qc\]](#).
- [67] L. Bernard, L. Blanchet, and D. Trestini, Gravitational waves in scalar-tensor theory to one-and-a-half post-Newtonian order, *JCAP* **08** (08), 008, [arXiv:2201.10924 \[gr-qc\]](#).
- [68] L. Bernard, E. Dones, and S. Moustakakos, Tidal effects up to next-to-next-to-leading post-Newtonian order in massless scalar-tensor theories, *Phys. Rev. D* **109**, 044006 (2024), [arXiv:2310.19679 \[gr-qc\]](#).
- [69] K. S. Thorne, Multipole Expansions of Gravitational Radiation, *Rev. Mod. Phys.* **52**, 299 (1980).
- [70] L. Blanchet, Post-Newtonian Theory for Gravitational Waves, *Living Rev. Rel.* **27**, 4 (2024), [arXiv:1310.1528 \[gr-qc\]](#).
- [71] E. Barausse, V. Cardoso, and P. Pani, Can environmental effects spoil precision gravitational-wave astrophysics?, *Phys. Rev. D* **89**, 104059 (2014), [arXiv:1404.7149 \[gr-qc\]](#).
- [72] B. J. Kavanagh, D. A. Nichols, G. Bertone, and D. Gaggero, Detecting dark matter around black holes with gravitational waves: Effects of dark-matter dynamics on the gravitational waveform, *Phys. Rev. D* **102**, 083006 (2020), [arXiv:2002.12811 \[gr-qc\]](#).
- [73] M. E. Pati and C. M. Will, PostNewtonian gravitational radiation and equations of motion via direct integration of the relaxed Einstein equations. 1. Foundations, *Phys. Rev. D* **62**, 124015 (2000), [arXiv:gr-qc/0007087](#).
- [74] F.-L. Julié and E. Berti, Post-Newtonian dynamics and black hole thermodynamics in Einstein-scalar-Gauss-Bonnet gravity, *Phys. Rev. D* **100**, 104061 (2019), [arXiv:1909.05258 \[gr-qc\]](#).
- [75] B. Shiralilou, T. Hinderer, S. M. Nissanke, N. Ortiz, and H. Witek, Post-Newtonian gravitational and scalar waves in scalar-Gauss-Bonnet gravity, *Class. Quant. Grav.* **39**, 035002 (2022), [arXiv:2105.13972 \[gr-qc\]](#).
- [76] G. Creci, T. Hinderer, and J. Steinhoff, Tidal response from scattering and the role of analytic continuation, *Phys. Rev. D* **104**, 124061 (2021), [Erratum: *Phys. Rev. D* **105**, 109902 (2022)], [arXiv:2108.03385 \[gr-qc\]](#).
- [77] L. D. Landau and E. M. Lifschits, *The Classical Theory of Fields*, Course of Theoretical Physics, Vol. Volume 2 (Pergamon Press, Oxford, 1975).
- [78] C. M. Will and A. G. Wiseman, Gravitational radiation from compact binary systems: Gravitational wave forms and energy loss to second postNewtonian order, *Phys.*

- Rev. D **54**, 4813 (1996), arXiv:gr-qc/9608012.
- [79] L. Blanchet, B. R. Iyer, C. M. Will, and A. G. Wiseman, Gravitational wave forms from inspiralling compact binaries to second postNewtonian order, *Class. Quant. Grav.* **13**, 575 (1996), arXiv:gr-qc/9602024.
- [80] W. P. Johnson, The curious history of faà di bruno's formula, *The American mathematical monthly* **109**, 217 (2002).
- [81] R. Epstein and R. V. Wagoner, Post-Newtonian generation of gravitational waves., *ApJ* **197**, 717 (1975).
- [82] M. Maggiore and A. Nicolis, Detection strategies for scalar gravitational waves with interferometers and resonant spheres, *Phys. Rev. D* **62**, 024004 (2000), arXiv:gr-qc/9907055.
- [83] C. Dalang, P. Fleury, and L. Lombriser, Scalar and tensor gravitational waves, *Phys. Rev. D* **103**, 064075 (2021), arXiv:2009.11827 [gr-qc].
- [84] A. Buonanno, B. Iyer, E. Ochsner, Y. Pan, and B. S. Sathyaprakash, Comparison of post-Newtonian templates for compact binary inspiral signals in gravitational-wave detectors, *Phys. Rev. D* **80**, 084043 (2009), arXiv:0907.0700 [gr-qc].
- [85] S. Droz, D. J. Knapp, E. Poisson, and B. J. Owen, Gravitational waves from inspiraling compact binaries: Validity of the stationary phase approximation to the Fourier transform, *Phys. Rev. D* **59**, 124016 (1999), arXiv:gr-qc/9901076.
- [86] L. Wade, J. D. E. Creighton, E. Ochsner, B. D. Lackey, B. F. Farr, T. B. Littenberg, and V. Raymond, Systematic and statistical errors in a bayesian approach to the estimation of the neutron-star equation of state using advanced gravitational wave detectors, *Phys. Rev. D* **89**, 103012 (2014), arXiv:1402.5156 [gr-qc].
- [87] T. Damour, Binary Systems as Test-beds of Gravity Theories, in *6th SIGRAV Graduate School in Contemporary Relativity and Gravitational Physics: A Century from Einstein Relativity: Probing Gravity Theories in Binary Systems* (2007) arXiv:0704.0749 [gr-qc].
- [88] B. Bertotti, L. Iess, and P. Tortora, A test of general relativity using radio links with the Cassini spacecraft, *Nature* **425**, 374 (2003).
- [89] J. S. Read, B. D. Lackey, B. J. Owen, and J. L. Friedman, Constraints on a phenomenologically parameterized neutron-star equation of state, *Phys. Rev. D* **79**, 124032 (2009), arXiv:0812.2163 [astro-ph].
- [90] G. Creci, Tidal properties of neutron stars in scalar-tensor theories of gravity: Mathematica code (2024).
- [91] J. Tran Thanh Van, T. Damour, E. Hinds, and J. F. Wilkerson, eds., *Perspectives in neutrinos, atomic physics and gravitation. Proceedings, 28th Rencontres de Moriond, 13th Moriond Workshop, Villars sur Ollon, Switzerland, January 30 - February 6, 1993* (Ed. Frontieres, Gif-Sur-Yvette, 1993).
- [92] F. Özel and P. Freire, Masses, Radii, and the Equation of State of Neutron Stars, *Ann. Rev. Astron. Astrophys.* **54**, 401 (2016), arXiv:1603.02698 [astro-ph.HE].
- [93] B. P. Abbott *et al.* (KAGRA, LIGO Scientific, Virgo), Prospects for observing and localizing gravitational-wave transients with Advanced LIGO, Advanced Virgo and KAGRA, *Living Rev. Rel.* **19**, 1 (2016), arXiv:1304.0670 [gr-qc].
- [94] D. Reitze *et al.*, Cosmic Explorer: The U.S. Contribution to Gravitational-Wave Astronomy beyond LIGO, *Bull. Am. Astron. Soc.* **51**, 035 (2019), arXiv:1907.04833 [astro-ph.IM].
- [95] Einstein telescope design report update 2020, https://gwic.ligo.org/3Gsubcomm/docs/ET-0007B-20_ETDesignReportUpdate2020.pdf.
- [96] S. Kawamura *et al.*, Current status of space gravitational wave antenna DECIGO and B-DECIGO, *PTEP* **2021**, 05A105 (2021), arXiv:2006.13545 [gr-qc].
- [97] E. E. Flanagan and S. A. Hughes, The Basics of gravitational wave theory, *New J. Phys.* **7**, 204 (2005), arXiv:gr-qc/0501041.
- [98] H. Sotani and K. D. Kokkotas, Stellar oscillations in scalar-tensor theory of gravity, *Phys. Rev. D* **71**, 124038 (2005), arXiv:gr-qc/0506060.
- [99] C. M. Will, *Theory and Experiment in Gravitational Physics*, 2nd ed. (Cambridge University Press, 2018).
- [100] M. Maggiore, *Gravitational Waves. Vol. 1: Theory and Experiments* (Oxford University Press, 2007).